Received: 8 February 2024 | Revised: 8 August 2024 | Accepted: 20 August 2024

DOI: 10.1111/bre.12896

RESEARCH ARTICLE

Basin Research IAS EAGE WILEY

Sediment flux variation as a record of climate change in the Late Quaternary deep-water active Corinth Rift, Greece

Mohamed A. Mohamed[1] | **Richard E. L. Collier**[1] | **David M. Hodgson**[1] | **Rob L. Gawthorpe**[2] | **Donna J. Shillington**[3] | **Martin Muravchik**[2] | **Dimitris Sakellariou**[4]

[1]Institute of Applied Geoscience, School of Earth and Environment, University of Leeds, Leeds, UK

[2]Department of Earth Science, University of Bergen, Bergen, Norway

[3]School of Earth and Sustainability, Northern Arizona University, Flagstaff, Arizona, USA

[4]Hellenic Center for Marine Research, Anavyssos, Greece

Correspondence
Mohamed A. Mohamed, Institute of Applied Geoscience, School of Earth and Environment, University of Leeds, Leeds LS2 9JT, UK.
Email: eemm@leeds.ac.uk

Funding information
The Research Council of Norway, DeepRift project number, Grant/Award Number: 308805; University of Leeds

Abstract

The value of deep-water sedimentary successions as reliable records of environmental change has been questioned due to their long response times and sediment pathways leading to complex responses to climatic change and tectonic signals over differing timescales. We studied the Gulf of Corinth, Greece, to test the value of deep-water stratigraphic successions as records of external controls on sediment flux in a setting with short response times and transport distances. The confinement of the rift basin allows for a near-complete accounting of clastic sediment volumes. The recent acquisition of high-resolution seismic reflection data, utilisation of International Ocean Discovery Programme Expedition 381 cores and a robust chronological framework, enable evaluation of the stratigraphy at a high temporal resolution. Combining borehole and high-resolution seismic reflection data, distinct seismic units can be correlated to multiple paleoenvironmental proxies, permitting quantification of sediment flux variation across successive glacial–interglacial cycles at ca. 10 kyr temporal resolution. Trends in average sediment flux since ca. 242 ka show ca. 2–9 times greater sediment flux in cooler glacials compared to warmer interglacial conditions. The Holocene is an exception to low sediment flux for the interglacials, with ca. 5 times higher rates than previous interglacials. The short and steep configuration of the Sythas canyon and its fan at the base of an active submarine normal fault results in deep-sea deposition at all sea-level stands. In contrast, adjacent canyon systems shut down during warm intervals. When combined with palynology, results show that periods of distinct vegetation re-organisation correlate to sediment flux changes. The temporal correlation of sediment flux to palynology in the Gulf of Corinth over the last ca. 242 kyr is evidence that variability of sediment supply is largely governed by climate-related changes in hinterland catchments, with sea-level and tectonics being second-order controls on sediment flux variability.

KEYWORDS

active rift basin, climatic variability, Corinth Rift, deep-water, Late Quaternary, sediment flux

1 | INTRODUCTION

The value of deep-water sedimentary successions as reliable archives of environmental change has been questioned (Heller & Paola, 1992; Jerolmack & Paola, 2010; Romans et al., 2016) due to the long distances and response times between climatic and tectonic perturbations in catchment areas and deposition in sedimentary basins. A temporal and spatial disconnect between source areas and sediment sinks is likely where sediment is transferred through multiple transient storage sites, resulting in the depositional signal becoming too 'shredded' to be used as an archive of environmental change (Allen, 2008b; Castelltort & Van Den Driessche, 2003; Sweet & Blum, 2016). For example, environmental signals can be fragmented, delayed or distorted during transport processes, making it challenging to accurately interpret these signals in the stratigraphic record (Jerolmack & Paola, 2010). Moreover, Tofelde et al. (2021) emphasise that different signal types need to be differentiated, and that the river response times, and signal propagation times need consistent terminology, when testing the transfer of perturbations into the stratigraphic record. They broaden the definition of 'signal' and classify signals by hydraulic grain size characteristics. This includes various types of 'times' related to signal arrival, lag and transfer.

Depositional systems active over intermediate timescales (10^2–10^6 years) can record both autogenic (intrinsic) and allogenic (extrinsic) signals (Romans et al., 2016). Some authors have explored the role of climate in controlling sediment transfer (Covault & Graham, 2010; Sweet & Blum, 2016) in intermediate timescales, recognising that the interplay of basin margin configurations and changes in climate can produce scenarios where increases or decreases in sediment flux can occur at any relative sea-level stage. This differs from short, historical timescales (ca. $<10^2$ years), characterised by its patchy coverage, that may not provide a comprehensive and continuous record of environmental changes over time and is thus unreliable in recording both autogenic and allogenic signals (Romans et al., 2016). Whereas longer time scales ($>10^6$ years) can also record autogenic signals, they present challenges in distinguishing between autogenic and allogenic signals due to the cumulative effects of multiple superimposed processes over extended periods (Hajek et al., 2012; Romans et al., 2016).

The eastern Gulf of Corinth in Greece is an active rift basin, characterised by rift margin drainage catchments adjacent to a deep basin, separated by normal fault systems that form a short and steep basin margin (Figure 1; Watkins et al., 2018). The eastern Gulf of Corinth facilitates an analysis of the development of deep-water, base-of-slope fans and the influence of intra-basinal faulting on depositional conditions characterised as 'underfilled' (Gawthorpe & Leeder, 2000). These base-of-slope submarine fans occur at the end of short sediment routeing systems, with limited sediment storage sites (Figures 1 and 2), and thus lend themselves to the preservation of environmental and tectonic signals (Romans et al., 2016; Sweet & Blum, 2016). Furthermore, the enclosed nature of the Gulf of Corinth facilitates the preservation of a more complete stratigraphic record compared to stratigraphic records on open continental margins such as of the Halten Terrace, offshore Mid-Norway (Elliott et al., 2021) and records that demonstrate how variable topography can contribute to an incomplete stratigraphic record (Fierens et al., 2019; Hinderer, 2012; Hofmann et al., 2006; Sømme et al., 2011).

Unravelling the links between external perturbations and the stratigraphic record has previously proven complicated within the Corinth Rift (Collier et al., 2000; Cullen et al., 2021; Watkins et al., 2018), due to the limits of chronological control and lithological calibration of seismic reflection data. The recent acquisition of cores from International Ocean Discovery Programme (IODP) Expedition 381 allows a chronological framework to be developed (Gawthorpe et al., 2022; Maffione & Herrero-Bervera, 2022), and new high-resolution seismic reflection data tied to the IODP Expedition 381 boreholes allows evaluation of submarine fan depositional systems and sediment flux variations in the evolving depocentre in the eastern Gulf of Corinth at a high temporal resolution (e.g. comparing ca. 10^4 years intervals since Marine Isotope Stage (MIS) 5). This study aims to evaluate the preservation of signals of Late Quaternary climatic and environmental change in a deep-water sedimentary succession. To achieve this, the following objectives will be

Highlights

- The eastern Gulf of Corinth has depositional conditions characterised as 'underfilled'.
- Sediment volumes calculated over the study area across glacial-interglacial cycles, including stadial-interstadial cycles.
- Sediment accumulation rates are up to 2–9 times higher during glacials than interglacials.
- The Holocene is an exception, with sediment accumulation rates ~5 times higher than other interglacial periods.
- The Sythas canyon sustained sediment supply to the deep sea during both glacial and interglacial periods.
- The basin configuration allows deep-sea deposition to occur at all sea-level stands.

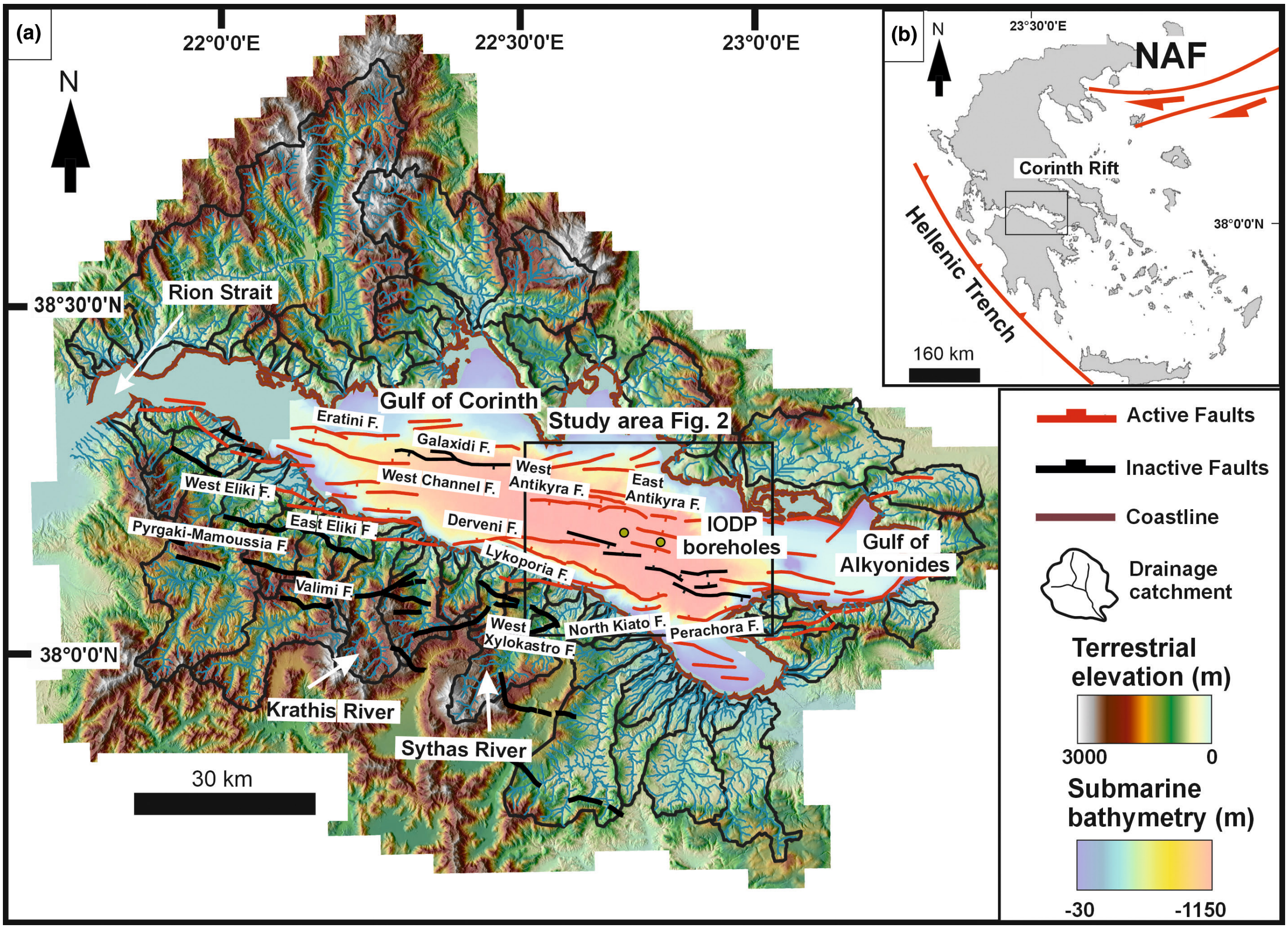

FIGURE 1 (a) Map of normal faults of the Gulf of Corinth Rift (this study and after Nixon et al., 2016), which includes both onshore and offshore topography at 5 and 50 m (Nixon et al., 2016) spatial resolution, respectively. The Onshore Digital Elevation Model (DEM) includes catchment and drainage networks after Pechlivanidou et al. (2019). Offshore normal faults (red) are associated with Late Pleistocene to Holocene rifting (faults with seabed morphological expression in solid red; faults propagating up towards the seabed in black). IODP borehole locations are shown as green dots. The inset box on the map (area of Figure 2) covers the study area in the eastern Gulf of Corinth, Greece. (b) Geodynamic setting of the study area. NAF, North Anatolian Fault.

addressed: (i) to quantify sediment flux from the hinterland source to the deep basin sink, (ii) to decipher the response of syn-rift sedimentation to quaternary climatic variability, during the last 242 kyr using high-resolution stratigraphic data from IODP Expedition 381 boreholes and new high-resolution mapping of seismic architectures, (iii) to develop a new conceptual model that links changes in sediment flux and climate, and (iv) to discuss the interplay of controls on base-of-slope fan system evolution and offshore sediment dispersal patterns.

2 | GEOLOGICAL SETTING

The Corinth Rift is one of the most tectonically active areas of continental rifting in the world, with high seismicity and north–south extension rates of ca. 5–15 mm/year from east to west (Bell et al., 2009; Briole et al., 2000; Clarke et al., 1998; Gawthorpe et al., 2018; Nixon et al., 2016). The rift system is relatively small, 100 km long, 40 km wide and up to 800 m deep, compared to other rift systems such as the East African, Red Sea and Baikal rifts (Nixon et al., 2016; Figure 1). The Corinth rift system comprises offshore (i.e. Gulf of Corinth, Alkyonides Gulf and Lechaion Gulf) and onshore (North Peloponnese) basins controlled by N- and S-dipping normal faults, and includes numerous now inactive faults (Bell, 2008; Ford et al., 2013, 2017; Gawthorpe et al., 2018; Hemelsdaël et al., 2017; Nixon et al., 2016, 2024) (Figure 1). The present fault network in the Gulf of Corinth is characterised by a series of right-stepping, en-echelon N-dipping normal faults along its southern margin (Eliki, Derveni, Lykoporia, Xylokastro, Kiato and Perachora Faults; Figure 1). Additionally,

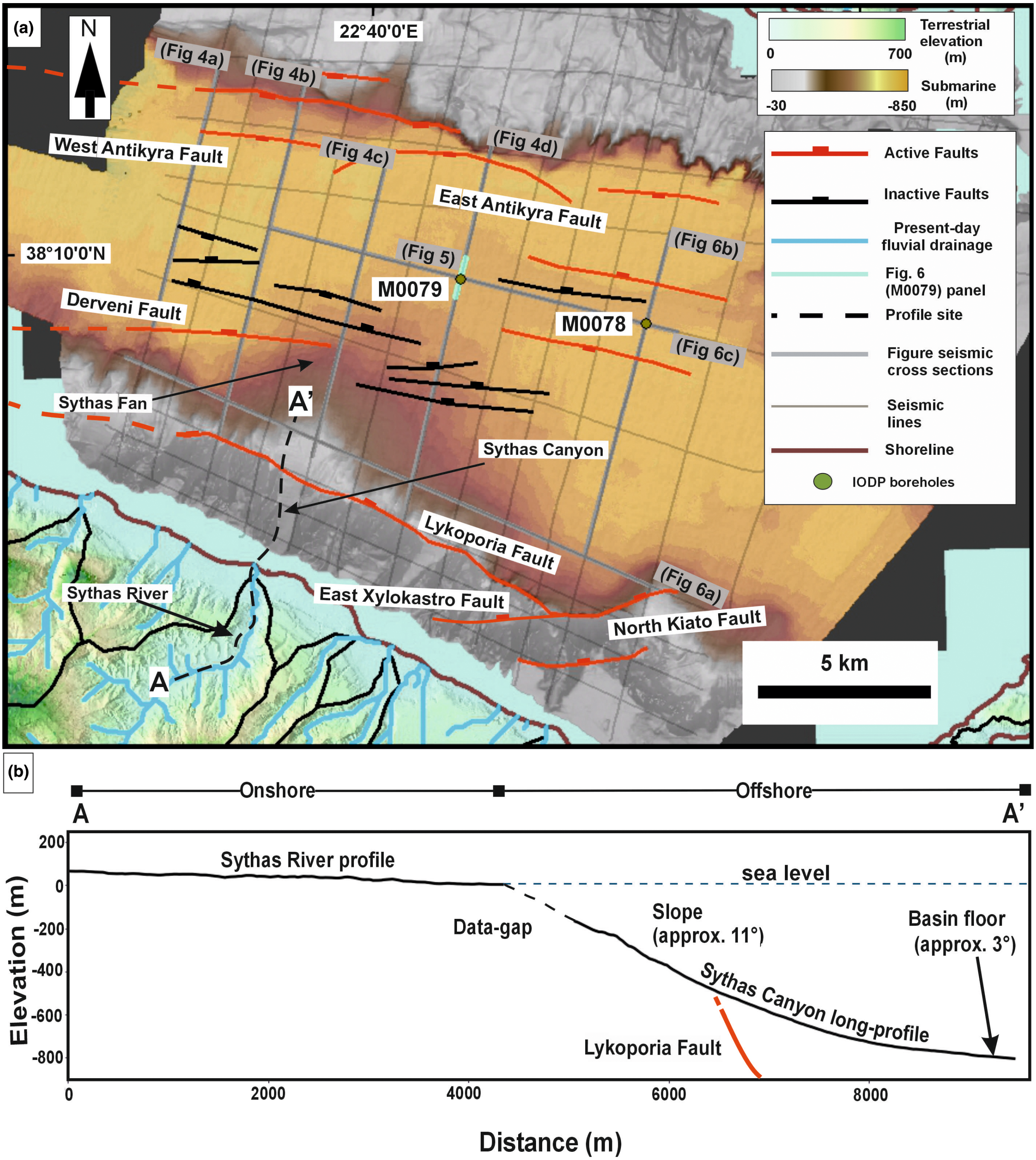

FIGURE 2 (a) Onshore DEM at 5 m spatial resolution adjacent to 30 m resolution bathymetry map highlighting short and sharp configuration of the Corinth source-to-sink system. Most N–S oriented canyons are connected to onshore drainage networks. Others are slope-confined. Onshore drainage networks courtesy of Pechlivanidou et al. (2019). Normal faults (red) are associated with Late Pleistocene to Holocene rifting (faults with seabed morphological expression in solid red; faults propagating up towards seabed in black; dashed fault continuations after Nixon et al., 2016). IODP borehole locations M0078 and M0079 are shown as olive-green dots. Pale green highlights the position of seismic in Figure 5. (b) Basin physiography along lines A–A', along the Sythas River and Sythas canyon; configuration consistent with simple bypass of sediments down the onshore–offshore transition.

there are major S-dipping faults along its northern margin (South Eratini, West Channel, Galaxidi and Antikyra Faults; Figure 1) with basement throw offsets exceeding ca. 700 m (Nixon et al., 2024).

The Corinth Rift underwent three distinct stages of structural evolution, evidenced by deposits found both onshore and offshore (Armijo et al., 1996; Ford et al., 2013, 2017; Gawthorpe et al., 2018; Nixon et al., 2016; Rohais & Moretti, 2017; Taylor et al., 2011). During the first rifting phase (Pliocene ca. 4–1.8 Ma), rifting was confined to the central and eastern northern Peloponnese (Gawthorpe et al., 2018; Nixon et al., 2016; Rohais & Moretti, 2017; Taylor et al., 2011). During the transition to the second rifting phase (at ca. 2–1.8 Ma), fault activity shifted northwards, relocating the rift depocenter in the region of the modern Gulf of Corinth. This shift was accompanied by a significant increase in extension rates (Ford et al., 2017; Gawthorpe et al., 2018). During the second rifting phase, the basin evolved into a more symmetrical rift due to the activity of north-dipping faults, such as those at Pyrgaki-Mamoussia, Valimi, West Xylokastro, Derveni and Lykoporia, and south-dipping faults, including the West Channel and Galaxidi structures (Ford et al., 2013; Gawthorpe et al., 2018; Nixon et al., 2016; Rohais et al., 2007; Figure 1). Further northward migration of fault activity occurred around 0.8 Ma, marking the end of the Pyrgaki, Mamoussia and Valimi Faults and the beginning of the East and West Heliki Faults (Gawthorpe et al., 2018; Hemelsdaël & Ford, 2016). In the eastern Gulf, increased uplift rates along southern margin faults transitioned the depositional system from a 'steady state' directly fed system (with Gilbert-type fan deltas) to an 'unsteady state' canyon-incised system along the active southern rift flank (Lykousis et al., 2007) (Figures 1 and 2). Fluvial networks with high erosional capacity persisted, incising and reworking older Gilbert-type delta deposits into the new hanging wall sinks (Ford et al., 2013, 2017). Deep basinal conditions off the southern margin in the eastern Gulf were dominated by transverse submarine fan deposits, built by sediment gravity flows, passing into mainly distal turbidites with some hemipelagic suspension fallout products in the hanging wall to the southern margin faults (Cullen et al., 2020; Gawthorpe et al., 2018; Rohais & Moretti, 2017). Between ca. 0.7 Ma and the present day, south-dipping faults in the Gulf of Corinth largely became inactive leading to the migration of depocentres into the immediate hanging walls of the major north-dipping normal faults along the southern shores of the Gulf of Corinth. Consequently, syn-rift packages thickened and were tilted southward and the rift transitioned to a more asymmetrical rift (Nixon et al., 2016). Deposits after ca. 0.7 Ma correspond to Seismic Unit 2 (of Nixon et al., 2016) and are analogous to the earlier rift successions now exposed onshore in the Peloponnese (Ford et al., 2013; McNeill et al., 2019).

A 60-m-deep sill across the Rion Strait now controls the connection of the Gulf of Corinth (GoC) to open ocean conditions (Perissoratis et al., 2000) (Figure 1). Pronounced cyclicity identified in the seismic facies of Seismic Unit 2 of Nixon et al. (2016) has been linked to intermittent marine incursions, interpreted to correlate to 100-kyr glacial–interglacial signals (Bell et al., 2009; Collier et al., 2000; Lykousis et al., 2007; McNeill et al., 2019; Moretti et al., 2003; Nixon et al., 2016; Perissoratis et al., 2000; Rohais & Moretti, 2017; Sakellariou et al., 2007; Watkins et al., 2018). Interpretation of lithostratigraphic packages (Collier et al., 2000; McNeill et al., 2019), observed downhole sedimentary facies (Gawthorpe et al., 2022) and sediment flux (Collier et al., 2000; Lykousis et al., 2007; Nixon et al., 2016; Watkins et al., 2018) have been used to corroborate the presence of this stratigraphic cyclicity.

3 | DATASET AND METHODS

The following data and methodology section documents efforts to interpret the eastern Gulf of Corinth basin fill using new bathymetry and seismic datasets acquired during cruises between 2020 and 2023 (Section 3.1) that are tied to IODP Expedition 381 boreholes. To enhance the interpretation of the basin fill spanning the last ca. 242 kyr, Section 3.2 documents the core-log-seismic integration (CLSI) techniques used to integrate IODP Expedition 381 borehole data with the new high-resolution seismic dataset. Section 3.3 outlines existing lithostratigraphic interpretations from borehole M0079 and the age model used in this study, and finally Section 3.4 outlines the steps taken to calculate sediment volumes and estimate sediment flux.

3.1 | Bathymetry and seismic reflection data

The new, high-resolution seismic reflection data used in this study consists of a 2D seismic reflection survey with an areal extent of ca. 337 km^2 (Figure 2) collected in 2020–2023 aboard the *R/V Aegaeo* research vessel. Data acquisition used a 40-in^3 airgun source and single-channel SIG seismic streamer (65 m length and 48 hydrophones at 1 m spacing). A standard sequence of post-acquisition seismic processing was applied using CodaOctopus Survey Engine software to enhance subsurface imaging and reduce the effects of multiples. This provided high-resolution imaging of the uppermost syn-rift succession (deposited since ca. 0.6 Ma; Nixon et al., 2016). Although the quality and coherency of the seismic reflection data decrease with depth, overall data quality is deemed good to moderate. Seismic reflection data are presented as zero-phase, following the Society of Exploration Geophysicists positive polarity convention, where a downward increase in acoustic impedance is represented by a positive reflection event with a peak shaded black. The dominant frequency ranges from 125 to 140 Hz, giving a vertical seismic resolution between 2.6 and 2.8 m (shallow) and 3.4–3.8 m (deep). Profiles acquired were parallel and perpendicular to the WNW–ESE trend of the basin margin with a line spacing of 0.5–1 km and a vertical sampling rate of 0.202 ms (TWT). Seismic interpretation, horizon mapping and attribute analysis were performed using Schlumberger's Petrel 2020™ software with the studied interval of interest spanning ca. 400–1800 ms (TWT).

Mapping of 2D seismic reflection data followed established seismic stratigraphic approaches (Catuneanu et al., 2009; Mitchum Jr et al., 1977), and builds on previous work in the Gulf of Corinth (Bell et al., 2009; Lykousis et al., 2007; Nixon et al., 2016; Taylor et al., 2011; Watkins et al., 2018), but using a higher temporal resolution. Seismic facies discrimination was based on variations in the amplitude, geometry, frequency and continuity of seismic reflectors which define six distinct seismic facies (Table 1). Seismic horizons were mapped using abrupt changes in seismic facies and attributes, and/or reflector terminations which allowed the recognition of ten basin-wide horizons (H1–H10) and the seabed (Figures 3–5) that define ten seismic stratigraphic units and sub-units (the seismic units being SU-A to SU-G; Figure 3). The study also presents a submarine multibeam bathymetry map (Figure 2), with coverage of ca. 68 × 22 km projected on WGS 1984 coordinates, which has 30 m grid-cell resolution, to capture the structure and geomorphology of the basin floor. Surface maps were edited and prepared using QGIS™ 3.28.0 and ArcGIS™ 10.6 software.

3.2 | Core-log seismic integration (CLSI)

CLSI was done by matching a synthetic seismogram calculated from Expedition 381 borehole data with the new, 2020–23 high-resolution seismic reflection data, following a similar method employed previously with lower resolution *Ewing* seismic data (McNeill et al., 2019a, 2019b) (see supplementary material for more information). This allowed: (i) lithostratigraphic interpretations from IODP boreholes to be correlated to prominent seismic reflection events (Gawthorpe et al., 2022), (ii) assessment of the impact of lithology on amplitude anomalies in stratigraphic levels of interest, (iii) accurate time-depth conversion and (iv) assessment of the depositional significance of interpreted horizons, facies and seismic units using combined well-seismic information to allow calibration of seismic character (seismic facies) to paleoenvironmental conditions within the Gulf – that is, marine versus non-marine/lacustrine conditions. CLSI is a critical step in applying a borehole-based age-depth model to the seismic reflection data (see the following section on the age-depth model).

3.3 | Borehole data and age-depth model

Successful drilling and coring were accomplished at 3 sites (M0078, M0079 and M0080) in October 2017, as part of the IODP Expedition 381 (McNeill et al., 2019a, 2019b; Shillington et al., 2018). Two sites (M0078 and M0079) were targeted and intersected by seismic lines within the study area, having been drilled and cored to 704 mbsf (metres below seafloor) and 610 mbsf, respectively (Figure 1). The sites provide a record of sedimentation and palaeoenvironmental change with resolution and penetration that constrains the recent phase of rifting (ca. 0.8 Ma). M0079 was particularly targeted for detailed analysis as it reveals an expanded and undisturbed marine/lacustrine succession (Seismic Unit 2 of Nixon et al., 2016; Lithostratigraphic Unit 1 of Gawthorpe et al., 2022). This permits correlation with 2D seismic reflection data (Gawthorpe et al., 2022; McNeill et al., 2019). Secondly, the location of the drill sites was identified as providing the best insight into the physiographic, stratigraphic and sedimentological makeup of the Gulf of Corinth. Gawthorpe et al. (2022) provide detailed visual core descriptions on drill core M0079, defining four primary sedimentary facies associations, based on their physical and sedimentary features (see Supplementary 1). In addition, detailed hole-to-hole correlations were facilitated by characterisation of lithostratigraphic sub-units of bioturbated, bedded and laminated intervals (see Supplementary 1). The alternation between fully marine and isolated sub-units is interpreted to reflect intermittent marine incursions through the Rion straits and an earlier connection through what is now the Corinth Isthmus during glacio-interglacial cycles (Gawthorpe et al., 2022; McNeill et al., 2019). We use a chronological framework that integrates IODP Expedition 381 magnetostratigraphy and micropalaeontology (McNeill et al., 2019; Sergiou et al., 2024), U/Th dating of aragonite laminations (Gawthorpe et al., 2022) and relative paleointensity analysis (Maffione & Herrero-Bervera, 2022). Preliminary age control of both drill sites (M0078 and M0079) used first and last appearance biostratigraphic events with age correlations facilitated by observed assemblages and qualitative abundance of microfossil groups (McNeill et al., 2019). We include biostratigraphic markers from Sergiou et al. (2024) to further enhance the chronostratigraphic framework of the study (Data S1—Section S1.6). Interpretations have

TABLE 1 Seismic facies and interpreted environments encountered in the Corinth Rift Late Quaternary basin fill, based on amplitude, geometries, frequency and reflector continuity.

Facies	Example	Description	Interpretation	Occurences
Channel_levee	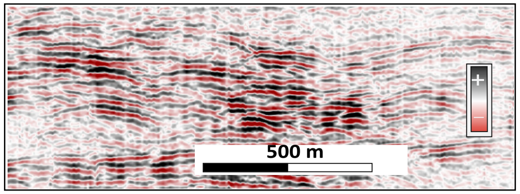	Low-moderate amplitude, sub-parallel to wavy reflectors with internal truncations, preserved as irregular 'gull-wing' channel-wedge geometries. Occur as vertically nested geometries (ca. 200–500 m) wide	Channel-wedge geometries are interpreted as a signature of a channel-levee combination. The nested, stacking-up configuration is typical of a channel complex set (e.g. Deptuck et al., 2003; Gee et al., 2007; Janocko et al., 2013; Mayall & Kneller, 2021)	Seismic units B, D, E, F and G
Erosionally-confined channels	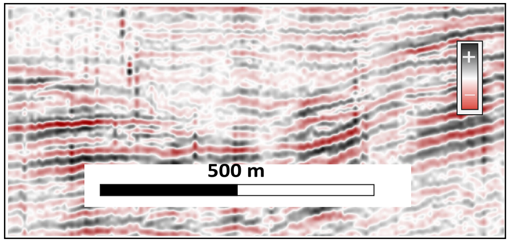	Low-moderate amplitudes, sub-parallel reflectors infilling u-shaped geometry with erosional truncation (width, ca. 200–500 m). Channel-fill onlap onto u-shaped basal contact	Erosional-confined channels with partial fills (e.g. Janocko et al., 2013; Posamentier & Kolla, 2003)	Seismic units D and G
Channelised lobes	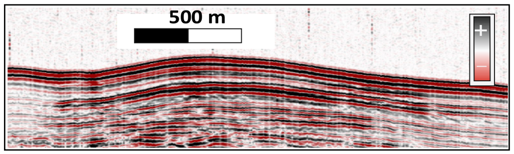	Moderate to high-amplitude continuous, parallel to sub-parallel, mounded-shaped reflector elements. Convexities of mounded-shaped elements are also channelized. Mounded reflector elements here are often associated with bidirectional downlaps	Mounded-shaped reflectors are interpreted as sheet-like geometries and fan lobes, deposited as precursors of the channels that bypass through them (e.g. Adeogba et al., 2005; Bakke et al., 2013; Posamentier & Kolla, 2003)	Seismic units E, F and G
Sediment waves	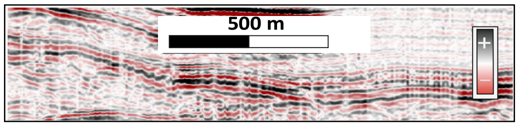	High-amplitude, symmetrical to asymmetrical wave-like reflectors with positive crests relative to the sea-floor	Interpreted as migrating sediment waves (e.g. Posamentier & Kolla, 2003; Wynn et al., 2002; Zhou et al., 2021)	Seismic units F and G
Background deposits	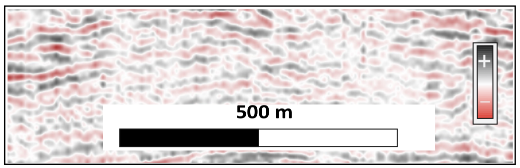	Low-moderate amplitude chaotic, poorly reflective, discontinuous reflector elements	Geometries suggest homogenous, poorly-reflective sediments which may be finer-grained sediments, dominated by suspension settling, for example (e.g. Stow & Mayall, 2000)	Seismic units B, D, E and G
Sheet turbidites	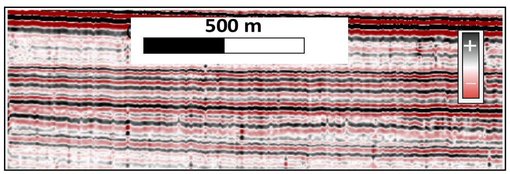	Moderate to high-amplitude, parallel to sub-parallel, low-angle, stacked sheet-like, continuous set of reflectors. Reflectors are seen as concave-upward curved seismic onlaps along the margins. Downlaping of older packages is also observed	Geometries are attributed to suspension fall-out deposition from unconfined gravity flows. Geometries are interpreted to represent composite depocentre-wide sandbodies (e.g. Marini et al., 2015; Piper et al., 1999; Posamentier & Kolla, 2003; Stow & Mayall, 2000)	Seismic units A, C, D, F and G

Note: A variety of seismic facies can occur within each unit in various abundances across the study area.

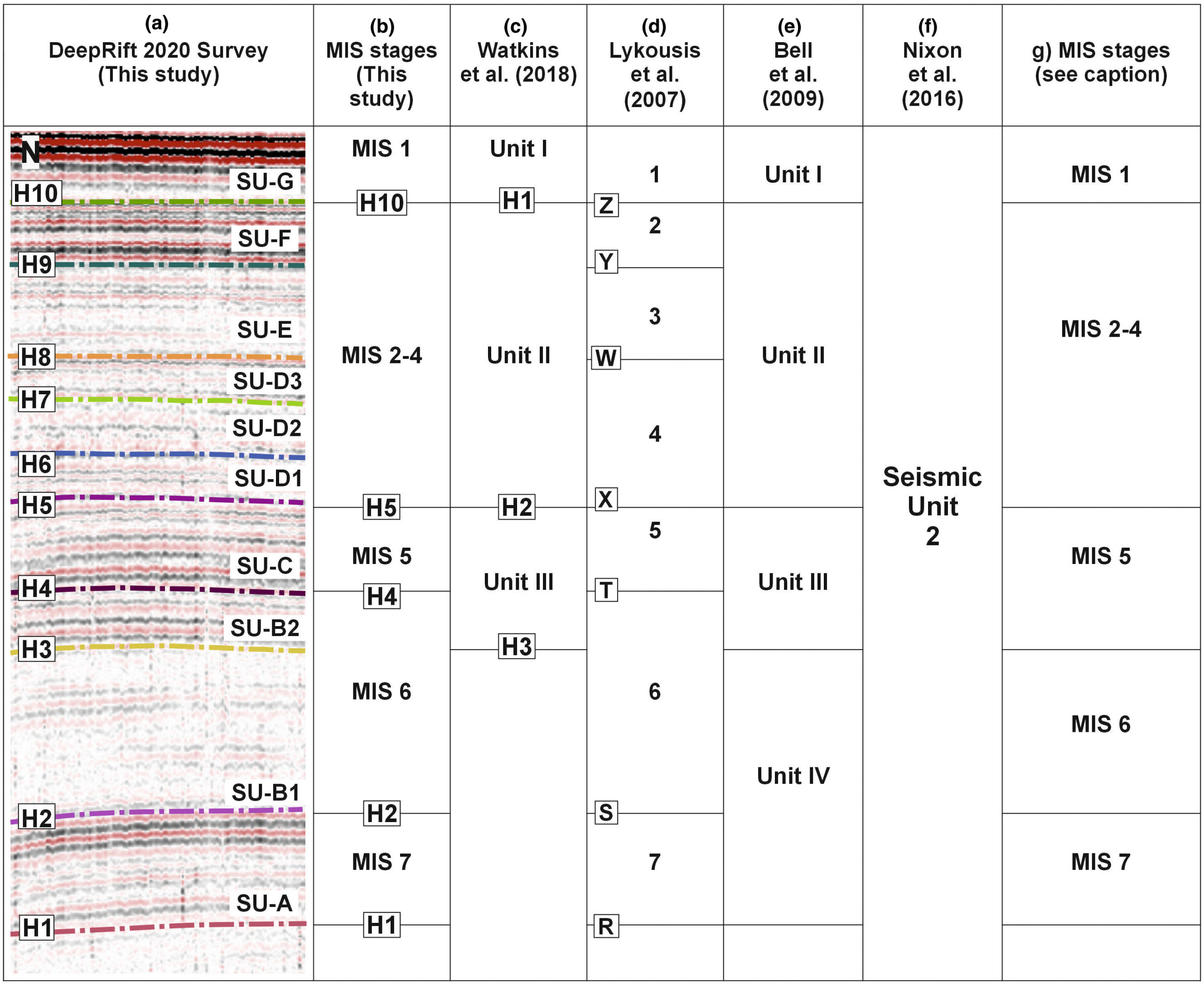

FIGURE 3 Summary of Gulf of Corinth seismic stratigraphy from this study compared to pre-existing stratigraphic frameworks. (a) High-resolution 2D seismic stratigraphy from this study and (b) correlated to Marine Isotope Stages (MIS). We also compare this study to interpretations from (c) Watkins et al. (2018), (d) Lykousis et al. (2007), (e) Bell et al. (2009) and (f) Nixon et al. (2016). Also incorporated are (g) MIS stage interpretations from previous studies Lykousis et al. (2007) and Watkins et al. (2018).

highlighted that the diversity and abundance of microfossil assemblages vary between intervals. Three samples from site M0079 were previously processed for Uranium/Thorium (U/Th) isotope analysis to help strengthen the age model in the upper part of the stratigraphy (since ca. 250 ka), as outlined in Gawthorpe et al. (2022). Critically, the sample previously dated at 88.2 ± 1.1 ka at 150 mbsf, corresponding to top MIS 5a, was excluded from our revised age model due to the recognition of detrital contamination (Sergiou et al., 2024).

3.4 | Quantifying sediment flux

The temporal variation in sediment accumulation in the Gulf of Corinth has been investigated by several studies (McNeill et al., 2019; Nixon et al., 2016; Watkins et al., 2018), but these have been hampered by either a lack of age control or seismic resolution. The acquisition of 2020–23 high-resolution seismic reflection data integrated with IODP Expedition 381 cores, with an updated chronological framework affords evaluation of sediment flux in the eastern Gulf of Corinth at higher temporal resolution than previously possible. Clearly defined and mapped seismic units with chronological constraints allow sediment volumes to be calculated over the study area for the last two glacial–interglacial cycles. The study follows others (Jobe et al., 2018; Romans et al., 2009; Sweet et al., 2020, 2021; Watkins et al., 2018) by utilising simple volumetric measurements of submarine fan and basin axis deposits. We derive (i) bulk volume V (m^3) and (ii) sediment volume V_s (km^3) for the isopach maps. We divide these measurements for each interval using their estimated ages (T) to derive (iii) time-averaged sediment flux, R (km^3/kyr), deposited in an interval. Seismically derived time-structure maps (TWT) extracted from stratigraphic intervals of interest were depth converted using a linear multi-layered velocity model developed based on the CLSI-derived velocities (see supplementary material) following the method of Schultz (1998) and Sofolabo et al. (2018) (Supplementary 2).

$$\text{Vinst }(z) = V0_{\text{top}} + (K)\text{Compact.} \tag{1}$$

The velocity model describes an increase in velocity function with depth using two parameters: (i) instantaneous velocities (z) at a reference surface ($V0$) against (ii) compaction gradient (K), defining the velocity rate increase with depth. Sediment volume estimates from isopach maps were computed for 10 seismic stratigraphic units (A–G and subunits), to allow extraction of sediment thickness. Volumes derived were subsequently accounted for porosity decay and the compaction trend of sediments of varying intervals using depth-porosity functions derived by Jobe et al. (2018).

$$\text{Sediment volume} = \text{Bulk volume} \times (1 - \text{porosity}). \tag{2}$$

The approach accounts for porosity by yielding volumes (zero-porosity) of fully compacted sediment (Jobe et al., 2018). Uncertainties include a lack of spatial precision in attributing porosity and velocity data across the study area, due to the distal location of the IODP drill sites. This could mean porosity and velocity values are not fully representative of lithological variation towards more proximal locations. However, due to the size of the study area this is considered a second order variation of the quantified grain volumes. Analysing isopach maps for volume estimation also eliminates spatial and temporal biases in volume derivation, as opposed to relying solely on one-dimensional sedimentary log data. Whilst we do not calculate sediment flux for the whole basin, analysing sediment flux variation within our well-defined study area in the eastern Gulf of Corinth offers insights into the variations in sediment flux across the entire Gulf of Corinth as this is an enclosed clastics sink.

4 | STRUCTURE AND GEOMORPHOLOGY OF THE EASTERN GULF OF CORINTH

Antecedent river networks orthogonal to the rift axis with lengths from ca. 1 to 50 km drain northward off

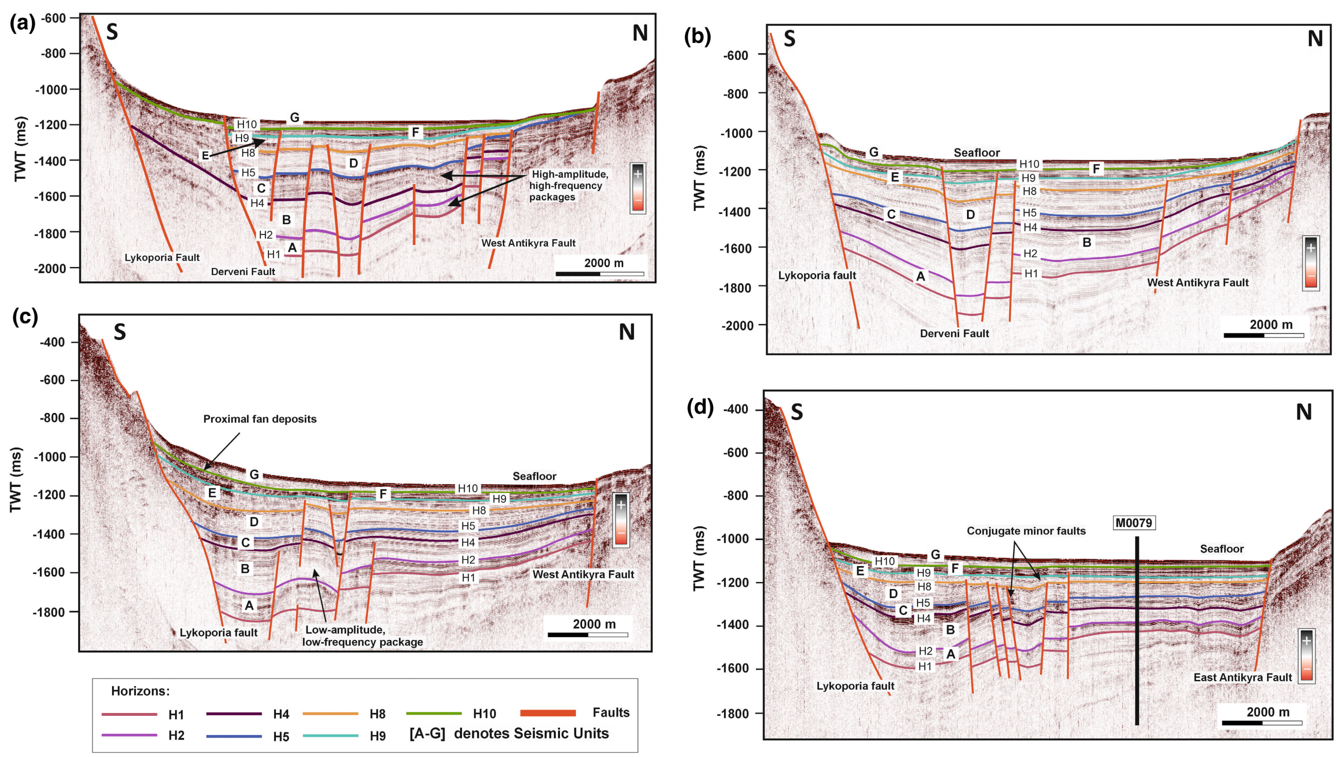

FIGURE 4 (a–d) Representative N–S oriented dip lines showing hanging wall stratigraphy. Seismic-line locations are shown in Figure 2. (d) Seismic cross-section highlights the location of IODP borehole M0079. Seismic facies occurrences combined with complex attributes were used to discriminate seven seismic units. Overall, this upper basin fill exhibits a south-tilted, wedge-shaped, asymmetric configuration reflecting control by steep southern margin faults. Also present are numerous intrabasinal faults.

the northern Peloponnese towards the Gulf of Corinth (Figure 1). The present-day southern margin of the eastern Gulf of Corinth exhibits an absent or narrow shelf, with a maximum width of ca. 2.5 km and a water depth of ca. −30 to −70 m (Figures 1 and 2). The morphology results in the direct alignment of onshore drainage channels with slope-confined and shelf-indenting canyons (Figure 2). Some of the thickest sediment accumulations and highest sedimentation rates in the eastern Gulf of Corinth study area are basinward of the Sythas River. Offshore, the main faults comprise the north-dipping East Xylokastro (EXF), Lykoporia (LKF), Derveni (DF), North Kiato (NKF) and Perachora (PF) Faults and the south-dipping, East- (EAF) and West-Antikyra (WAF) Faults (Figures 1 and 2). The East and West Xylokastro fault segments sit in the footwall of the LKF (Brooks & Ferentinos, 1984; Cullen et al., 2021; Gawthorpe et al., 2018; Higgs, 1988; Moretti et al., 2003; Nixon et al., 2016; Stefatos et al., 2002; Taylor et al., 2011). Southward tilting and thickening of 'syn-rift' deposits record the overall displacement and activity of the southern margin border faults (Figure 4a–d). Maximum total sediment thicknesses (1100–2000 ms TWT) are observed in the immediate hanging wall of the EXF and LKF faults (Nixon et al., 2024). The main depocentre includes numerous previously unmapped north- and south-dipping intrabasinal and conjugate minor faults that controlled thickness changes in syn-rift sequences (Figures 4a–d and 6b,c). The presence of conjugate faults and intrabasinal structures has led to significant accommodation space in the hanging wall of the DF (Figures 1 and 2). The northern margin comprises a series of less significant and less active and buried inactive faults (Bell et al., 2009; Nixon et al., 2016). Uplifted horst blocks in the main depocentre are bounded by north- and south-dipping faults (notably in Figure 6b).

5 | SEISMIC STRATIGRAPHY

Seismic interpretation allowed discrimination of Seismic Units (SU) A to G based on a combination of seismic facies, geometries and attributes, which are delineated by seven of the ten mapped seismic horizons (Figures 5 and 6). Seismic horizon and unit interpretations are supported by IODP lithofacies data from borehole M0079 (Gawthorpe et al., 2022). Horizons (H) 3, 6 and 7 are picked based on mappable reflectors that do not mark basin-wide vertical changes in seismic facies but allow sub-division of SU-B and SU-D providing greater stratigraphic resolution in subsequent sediment volume calculations. H3–10 are mapped across the study area, but seismic H1 and H2 are picked with lower confidence in the most proximal (southern) parts of profiles due to poor data quality and cut-offs by faulting at those depths (Figure 6a). Seismic Units A to G are all contained within Seismic Unit 2 of Nixon et al. (2016). The subsequent section describes and interprets the basin fill of the eastern Gulf of Corinth, encompassing SU-A to G, spanning the last ca. 242 kyr.

5.1 | Seismic Unit A (SU-A): Moderate- to high-amplitude, moderate-frequency basin fill

5.1.1 | Observations

Seismic Unit A is bounded at its base and top by H1 and H2, respectively. Overall, SU-A forms a southward-tilted fault-bounded wedge. Along- and across-fault thickness variations are evident in E–W trending depocentres within SU-A, particularly near north-dipping basin-bounding faults. Seismic Unit A is thickest in depocentres located in the immediate hanging wall of the Derveni and Lykoporia Faults and thins towards bathymetric highs along both margins (see Figure 4).

Seismic Unit A is punctuated by numerous intrabasinal structures (Figure 7a) and has a maximum time-thickness of ca. 150 ms TWT (Figure 4c). The unit has a time-thickness of 50 ms TWT around site M0079 (Figures 4 and 6). Seismic Unit A thins and onlaps onto the intrabasinal horst near site M0078 and associated intrabasinal highs (Figure 7a). Near site M0078, SU-A thickens along the immediate hanging walls of both the northern and southern faults bounding the horst (Figure 6b).

Overall, SU-A comprises moderate- to high-amplitude, moderate-frequency, parallel continuous reflectors separated in places by a thin opaque interval (Figures 4 and 6). Strike and dip profiles show SU-A to be dominated by sheet-like geometries (Table 1). Seismic Unit A corresponds to a depth range of 270–310 mbsf in M0079, where the unit comprises in detail (and following the facies terminology of Gawthorpe et al., 2022) sub-millimetre to millimetre-thick laminated mud beds and highly bioturbated deposits (average centimetres to tens of centimetres thick) interbedded with graded bed types (Figures 3 and 5 and Data S1).

5.1.2 | Interpretations

Sediment volumes and displacement variations in proximal strike profiles suggest sediment routeing was controlled by the Lykoporia and Derveni Faults (Figure 7a). Growth of E–W trending depocentres and their time-thickness variations of up to ca. 150 ms TWT are ascribed to activity along the Lykoporia, Derveni and S-dipping intrabasinal faults. Tilting of SU-A strata around the

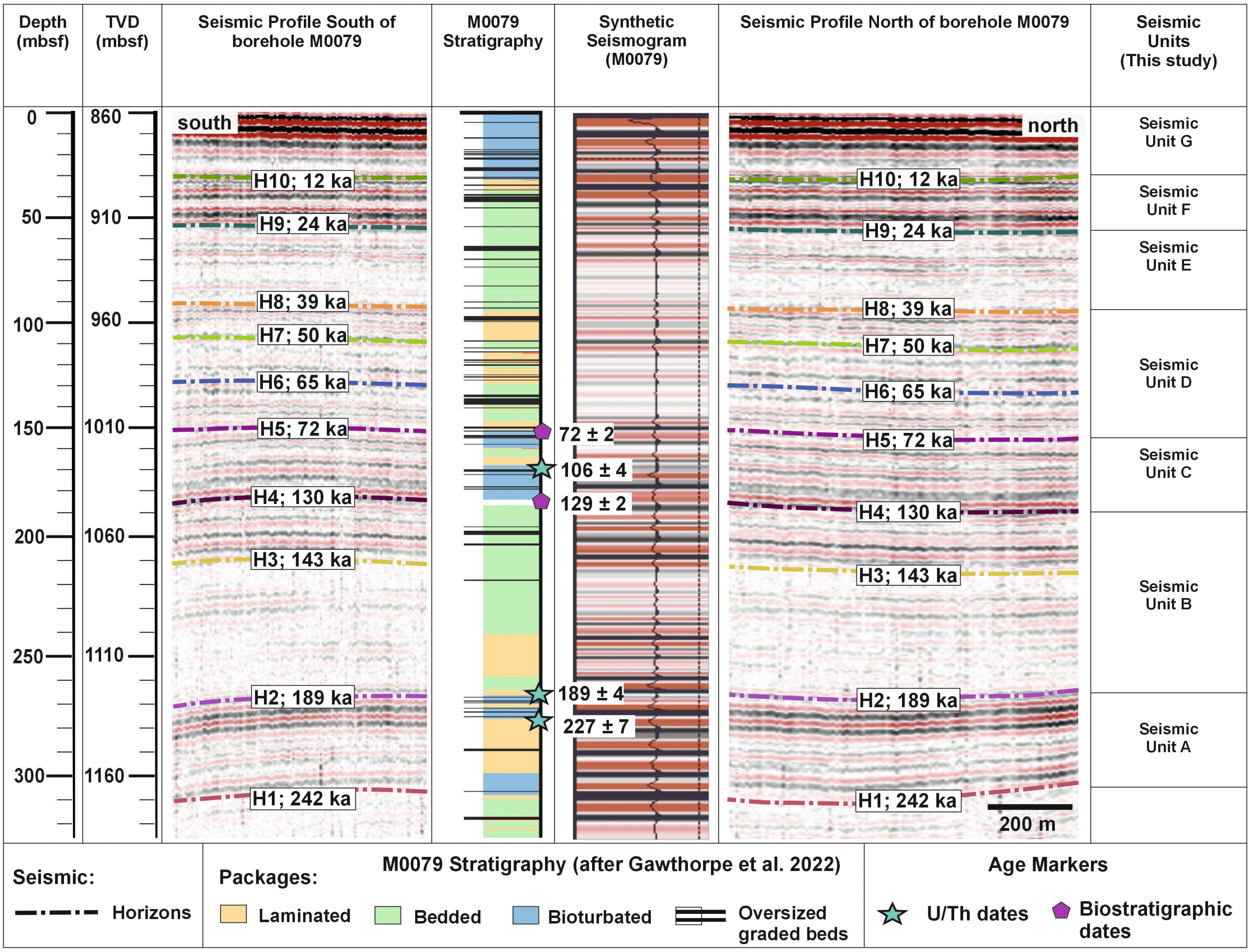

FIGURE 5 Seismic-well tie (in depth, mbsf and TVD) across site M0079 (location shown in Figure 2), tying onto the lithological framework established in Gawthorpe et al. (2022). Seismic section is shown in pale green in Figure 2. (A) We distinguish ten seismic intervals (bounded by horizons H1 to H10). Panel of M0079 lithostratigraphy from Gawthorpe et al. (2022), simplified stratal packages (to right) and the synthetic seismogram (to right) which allow correlation of lithostratigraphy with prominent seismic-reflection events in the basin fill. Also shown to the right is a summary of the seven seismic units (SU-A to SU-G) (as utilised in Figures 4 and 6) with variable high and low reflectivity. We incorporate biostratigraphic and U/Th markers from Sergiou et al. (2024) and Gawthorpe et al. (2022) to enhance the chronology of borehole M0079 over the past ca. 242 kyr.

intrabasinal horst near site M0078, where SU-A is observed to thin and onlap onto the footwall crest of the intrabasinal horst, is attributed to displacement variations along and between the horst-bounding-faults.

Sediment supply in SU-A was from fault-transverse sediment transport systems and may also have included input along a km-wide axial trough in the hanging wall to the Derveni Fault from the River Krathis to the west of the study area (Figure 7a). The widespread occurrence of extensive, moderate- to high-amplitude sheet-like geometries, interpreted as sheet-turbidites (Table 1), and the lateral thickness variations of the seismic unit (Figure 7a) indicates that SU-A was largely distal to canyon-sourced submarine fan systems. The transition from a non-marine bedded package to a marine bioturbated interval (Figure 5) is marked by Horizon 1 and corroborates that deposition of SU-A was mostly under open basin conditions with well-oxygenated marine waters and a diverse infaunal presence (Gawthorpe et al., 2022). Seismic Unit A consists of three parts at the site of M0079 (Figure 5). The highly-reflective base of SU-A corresponds to a bioturbated marine interval, the more opaque central layer correlates with mainly laminated non-marine beds and the highly reflective upper layer is dominated by marine bioturbated strata. The seismic response of SU-A is linked to deposition and a prevalence of stratified, oversized graded beds that are typically several tens of centimetre thick (Gawthorpe et al., 2022). Although bioturbation is present in SU-A, stratified graded beds, consisting of the coarser sediments, remain relatively undisturbed and generate reflectivity in this interval.

5.2 | Seismic Unit B (SU-B1 and B2): Low-amplitude, low-frequency divergent fill

5.2.1 | Observations

Seismic Unit B is bounded at the base and top by H2 and H4, respectively, and has a wedge-shaped geometry that thickens southward towards the Lykoporia and Derveni Faults (Figure 4). Horizon 3 subdivides SU-B into SU-B1 and SU-B2. Seismic Unit B preferentially infills depocentres adjacent to the Derveni and Lykoporia Faults with maximum time-thicknesses of up to ca. 200 ms TWT for SU-B1 and ca. 150 ms TWT for SU-B2, respectively (Figures 5 and 7b,c). A number of active faults, including the East Antikyra Fault, bound the northern margin of the SU-B depocentre. Seismic Unit B is also punctuated by numerous intrabasinal structures (Figure 7b,c), and varies in thickness, with extensive growth strata along and across the basin. Thickening in SU-B1 is also prominent in the immediate hanging wall of both faults bounding the horst near site M0078. Sediment accumulation and supply during SU-B are ascribed to contributions from multiple fault-transverse sediment transport pathways entering the hanging wall of the Derveni and Lykoporia Faults (Figure 7b,c).

In general, SU-B comprises subparallel, low-amplitude, low-frequency reflectors (Figures 4 and 6), with the exception of SU-B2 (upper SU-B), which appears as a continuous interval with moderate- to high-frequency reflectors (Figure 5). Locally, SU-B forms patches of irregular moderate amplitude reflections in proximal locations (Figure 4a–d). Proximal E–W seismic profiles are interpreted to include vertically stacked channel-levee geometries (ca. 200–500 m wide, ca. 50 ms in time-depth) (Table 1, Figure 6a). Segments of the channel-levee geometries are seen to gradually flatten out and thin towards distal parts of the basin into low-amplitude, low-frequency, discontinuous reflectors (Table 1). Seismic Unit B corresponds to the depth range of 185–270 mbsf in M0079 which mainly comprises bedded packages of non-marine, graded and homogeneous mud beds that individually are ca. 1–2 cm thick (Gawthorpe et al., 2022; Figure 5). The correlation of SU-B to the lithostratigraphy of Gawthorpe et al. (2022) also indicates that a laminated package occurs in SU-B between 240 and 260 mbsf in M0079 and is made up of sub-millimetre to millimetre-thick laminated mud beds. Oversized graded beds (average ca. 1 m thick) are present but cluster in SU-B2 (upper SU-B). Bedded packages are described as lacking intense bioturbation and are often under- and overlain by laminated packages.

5.2.2 | Interpretations

Significant thickening and tilting of SU-B against the Derveni and Lykoporia Faults indicates syn-sedimentary fault activity. Faulting and offsets throughout SU-B, particularly SU-B1, point towards activity associated with all north- and south-dipping faults (Figure 7b,c). Fault-related depocentre associated with the Derveni and Lykoporia Faults significantly restricted sediment accumulations to proximal locations in SU-B2.

Isopach variations suggest depositional activity throughout SU-B can be ascribed to supply by multiple fault-transverse, and potentially from axial, sediment transport systems west of the Derveni Fault (Figure 7b,c). The presence of stacked fault-transverse, channel-levee geometries (Table 1) interpreted as levee-confined channels in E–W strike profiles (Figure 6a), suggests aggradation and flow stripping/overspill by turbidity currents, and relatively mud-rich flows building external levees and providing bank cohesion (McHargue et al., 2021). Flattening of seismically resolvable channel-like geometries northwards implies a gradual basinward loss of confinement.

Based on higher amplitudes in proximal sites, we propose that coarse-grained sediments entered from hinterland catchments but were deposited against intervening intrabasinal structures. We interpret the extensive and unconfined nature of low-amplitude, low-frequency, discontinuous background deposits in the central and north-eastern parts of the basin to represent low-energy environments dominated by suspension settling from unconfined, waning low-density turbidity currents.

Seismic response and opaque SU-B character are interpreted to result from the homogeneity of cm-scale thin-bedded graded beds, homogenous bed-types and sub-millimetre to millimetre-thick mud beds that fall below seismic resolution, except for SU-B2 where there are packages of thicker graded beds (Gawthorpe et al., 2022; Figure 5). Overall, SU-B lacks individual beds thick enough to form any reflectivity (Figure 5), but graded bed packages give the moderate to higher amplitudes present in SU-B2 (Figure 3). The lack of intense bioturbation and absence of associated marine fauna and microfauna imply SU-B to be a predominantly non-marine interval. Compositional characteristics and correlation to bed types suggest deposition of SU-B in dysoxic basinal waters through contributions from lofted plumes and waning low-density turbidity currents during a time when the Gulf Corinth was isolated to semi-isolated from open ocean conditions (Gawthorpe et al., 2022).

5.3 | Seismic Unit C (SU-C): Moderate- to high-amplitude, moderate- to high-frequency basin fill

5.3.1 | Observations

Seismic Unit C is bounded at the base and top by H4 and H5, respectively. Overall, SU-C is preserved as a faulted,

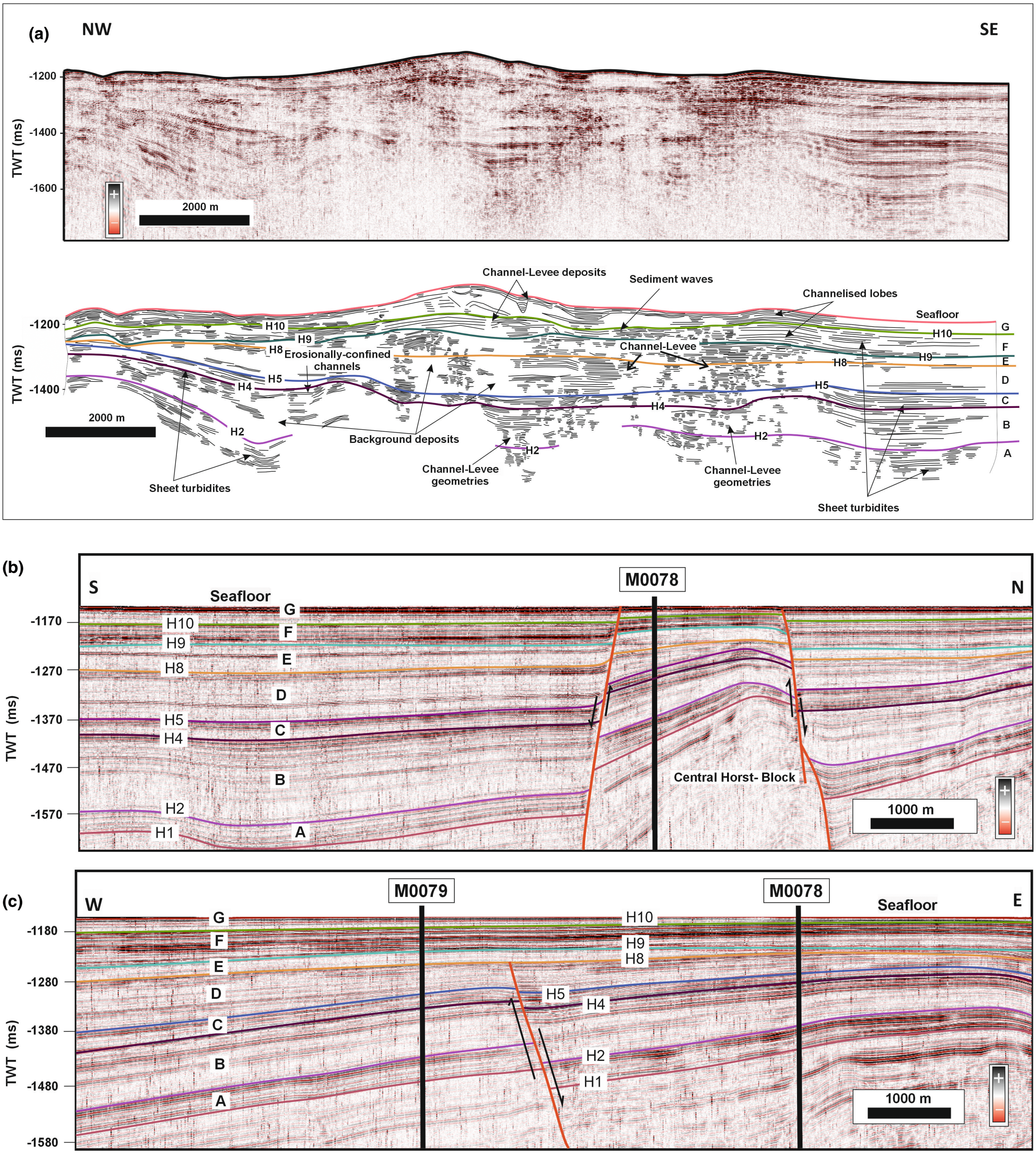

FIGURE 6 (a) Proximal strike line showing geometries and facies used to construct the seismic stratigraphic framework. Uninterpreted and interpreted seismic sections, located in Figure 2, highlight the variety of seismic facies geometries listed in Table 1. (b) Annotated dip-line oriented S–N across borehole M0078, with intrabasinal faults contributing to observable thickness changes within the eastern Gulf. (c) Annotated W–E oriented strike line intersecting boreholes M0078 and M0079. Seismic-line location is shown in Figure 2.

wedge-shaped parallel to sub-parallel, continuous moderate- to high-amplitude, high-frequency reflector package. In the western part of the study area, SU-C is heavily faulted and punctuated by a series of localised intrabasinal structures (Figure 7d). Thickness variation and growth strata within SU-C are observed in the immediate hanging wall of the Derveni Fault where SU-C records substantial time-thicknesses up to ca. 135 ms TWT (Figure 7d). Near site M0079, SU-C is thinner (ca. 35 ms TWT) than the overlying and underlying relatively low-amplitude SU-B and SU-D (Figures 4 and 6).

The package converges and thins towards the northern margins of the basin with simple onlaps. Less prominent faults and monocline flexures are observed in the subsiding NW confines of the study area, corroborating previous observations (Lykousis et al., 2007; Nixon et al., 2016). Seismic Unit C is dominated by sheet-like geometries (Table 1) with good, km-scale longitudinal continuity extending across the basin floor. Seismic Unit C is dominated by bioturbated, mud- and fossil-dominated bed-types (average centimetres to tens of centimetres thick) from 150 to 185 mbsf (see Supplementary 1 for depth conversion data) (Figure 5). Correlations to the lithostratigraphy indicate that the marine bioturbated packages in SU-C include oversized graded bed-types (Gawthorpe et al., 2022; Figure 5). A near-opaque interval from ca. 160 to 168 mbsf corresponds to non-marine mud packages in the lithostratigraphy.

5.3.2 | Interpretations

Sediment accumulations and growth strata in the E–W trending depocentre suggest syn-sedimentary fault activity, and sediment routeing may have included an axial element, with input from the west, from the Krathis River into the hanging wall of the Derveni Fault (Watkins et al., 2018; Figure 7d). The lack of significant sediment accumulations away from the Derveni Fault is ascribed to a reduction in sediment flux, due to less hinterland supply and/or inactive fault-transverse sediment transport systems. The dominant presence of sheet-like moderate- to high-amplitude reflectors interpreted as sheet turbidites (Figures 4 and 6) and thickness variation in the hanging wall of the Derveni supports SU-C as being linked to modest inputs from transverse canyon-linked stacked fan systems and potential sources from the west such as the Krathis River.

The presence of muddy and coarser-grained graded bed-types suggests low-density turbidity currents and hemiplegic sedimentation but possibly also high-density turbidity currents in more proximal locations (Piper et al., 1999; Stow & Mayall, 2000). The acoustic reflectivity of SU-C is linked to stacked oversized graded beds (Figure 5) composed of coarser-grained sediments that were sufficiently undisturbed and thick enough to contribute to reflectivity. The stratigraphic change marked by H4 from non-marine bedded to marine bioturbated deposits (Figure 5) is consistent with the deposition of SU-C under open basin conditions with well-oxygenated marine waters and a diverse infaunal presence – other than in the limited non-marine packages at ca. 160–168mbsf.

5.4 | Seismic Units D (SU-D1, D2 and D3): Low- to moderate-amplitude, moderate-frequency divergent fill

5.4.1 | Observations

Seismic Unit D is bounded above and below by undulating H5 and H8. The unit forms a northward- and southward-tilted wedge-shaped configuration, downfaulted towards the basin-axis (Figure 4). H6 and H7 subdivide SU-D into SU-D1, SU-D2 and SU-D3, from base to top (Figure 3). Growth strata and thickening are observed in SU-D1 and SU-D2 in the immediate hanging wall on both fault-bounding sides of the horst near site M0078 (Figures 6b and 7e,f). Elsewhere, SU-D1 and SU-D2 converge and thin towards the northern margin of the basin. North-dipping basin-bounding faults contribute to along- and across-fault thickness variations in E–W trending depocentres in SU-D1 and SU-D2 (Figure 7e,f). The maximum time-thickness of SU-D1 and SU-D2 is ca. 70 ms TWT and ca. 95 ms TWT respectively. A noticeable eastward thickening is evident in the main depocentre from SU-D1 to D2, on the hanging wall side of the Derveni Fault (Figures 4 and 6) and towards the Lykoporia Fault (Figure 7e,f). Seismic Unit D3 does not reveal significant thickness variation and has a maximum observed time-thickness of ca. 40 ms TWT (Figure 7g).

Overall, SU-D comprises subparallel, low- to moderate-amplitude, moderate-frequency reflectors (Figures 4 and 6), with minor differences in frequency and continuity; SU-D2 comprises low-frequency and semi-continuous reflectors, whereas SU-D1 and SU-D3 comprise higher frequency and continuous reflector intervals (Figure 5). Furthermore, SU-D is dominated by prominent fault-transverse, confined channel-forms (ca. 500 m wide, ca. 40 ms in time-thickness) and channel-levee geometries (ca. 200–500 m wide, ca. 50 ms in time-thickness) (Table 1). These geomorphic elements are preserved as vertically nested in a threefold hierarchy from isolated bodies (ca. 50 m wide and ca. 10 ms in time-thickness) to complex-sets (ca. 500–1000 m wide, ca. 50 ms in time-thickness) (Figure 6a). Continuation and incision of channel-like geometries are subtle or not observed beyond the proximal part of the basin, more than ca. 3 km north of the Lykoporia Fault. E–W strike profiles show segments of these channel-like geometries transition and thin down-dip into low- to moderate-amplitude, moderate-frequency, semi-continuous reflectors (Table 1). Seismic Unit D lies from ca. 150 to 90 mbsf at borehole M0079 (Figure 5) and corresponds to bedded packages from ca. 150 to 130 mbsf which consist of graded and homogeneous mud-beds, and mainly laminated bedding packages from ca.130 to 90 mbsf. Seismic Unit D also includes graded beds, which are normally-graded medium sand to silt to homogenous mud beds (Gawthorpe et al., 2022; Figure 5). There is a higher frequency and thickness of graded beds within SU-D than the preceding seismic units.

5.4.2 | Interpretations

The wedge-shaped geometry and thickening of SU-D in the basin axis indicate that S-dipping intrabasinal structures were significantly active in this area at this time (Figure 7e–g). This is corroborated by growth in the E–W trending depocentre, which demonstrates increasing sediment accumulation towards the east from SU-D1 to SU-D2. The lack of thickness changes in SU-D3 could suggest relative tectonic quiescence and/or near shut-down of supply from fault-transverse sediment transport systems (Figure 7e–g).

The dominance of fault-transverse stacked channel-forms suggests the prevalence of submarine channel belts in SU-D1 and SU-D2 (Figure 6a) that can be traced up-dip to canyons. Down-flow continuation of fault-transverse sediment transport systems directed sediments towards the basin axis. The presence of erosionally confined channel forms is a product of recurring erosional flows.

Channel-levee geometries (Table 1) are interpreted as levee-confined channels as seen in E–W strike profile, indicative of aggradation, flow stripping and overspill by turbidity currents.

The moderate reflectivity in SU-D can be attributed to the frequent occurrences of thin and oversized graded beds (terminology of Gawthorpe et al., 2022), as well as homogeneous mud beds (Figures 4 and 6). Seismic response in SU-D is also attributed to a scarcity of thick stratified intervals, which were restricted in proximal sites compared to the finer-grained sediments interpreted near site M0079. The transition from SU-C to SU-D, to bedded and laminated packages with only minor bioturbation, signifies the deposition of SU-D in non-marine basinal waters during a time when the Gulf of Corinth was isolated to semi-isolated from open ocean conditions (Gawthorpe et al., 2022; McNeill et al., 2019).

5.5 | Seismic Unit E (SU-E): Low- to moderate-amplitude, moderate-frequency divergent fill

5.5.1 | Observations

Seismic Unit E is bounded at its base and top by H8 and H9 respectively and forms faulted, north and south-tilted wedge-shaped configurations towards the Lykoporia Fault (e.g. Figure 4c) or towards basin-axis (e.g. Figure 4b). Seismic Unit E thickens in the hanging wall of south-dipping intrabasinal faults (Figure 7h), reaching a maximum time-thickness of up to ca. 80 ms TWT (Figure 4), and is ca. 40 ms TWT thick near borehole M0079 (Figures 4 and 6). Mapped intrabasinal structures are also seen to influence SU-E thicknesses in the hanging walls of the West Antikyra Fault and the southern side of the horst near site M0078 (Figures 1 and 7h).

Seismic Unit E is identified by its overall sub-parallel opaque, low-amplitude, moderate-frequency character (Figures 3 and 5). E–W strike profiles highlight the presence of fault-transverse, channel-forms bounded by wedges (ca. 500 m wide and ca. 40 ms in time-thickness) (Table 1), which are vertically nested (Figure 6a). An increase in wave-like features associated with channel-levee geometries (Table 1) is observed towards the transition to SU-F. Overall, proximal seismic facies geometries (Table 1) are observed to transition northwards, in N–S dip profiles, into opaque, low-amplitude, moderate-frequency reflector elements (Table 1). Seismic Unit E is predominantly made up of bedded bed-types from ca. 90 to 55 mbsf. The unit does however include thinly bedded graded beds (Figure 5) and occasional oversized graded beds.

5.5.2 | Interpretations

Thickness variation and growth strata in E–W trending depocentres imply a strong fault control on accommodation generation in SU-E. Fault-related topography associated with intrabasinal structures preferentially restricted sediment accumulation to proximal locations and was sufficient to limit sediment dispersal towards the NW of the study area (Figure 7h). Occurrences of fault-transverse stacked channel-forms suggest that SU-E is dominated by submarine channel belts up to ca. 2.5 km from the basin-bounding faults in the south (Figure 6a).

Vertically stacked submarine channel-belts in proximal settings support an interpretation of sediment transport in high-energy environments on a relatively steep gradient basin floor (Beaubouef, 2004; Sprague et al., 2002). In addition, aggradation and oblique sidestepping of channel-forms is interpreted as a response to changing in flow pathways or to changes in depositional topography (Gardner et al., 2003). Channel-levee geometries and sediment waves point towards overspill and flow-stripping (sensu, Posamentier & Kolla, 2003; Table 1). Down-dip shallowing and widening of channel-like geometries imply a gradual loss of confinement at channel mouth transition zones (Hodgson et al., 2022) as sediments are transported towards the more distal basin floor. The extensive and unconfined nature of low-amplitude, low-frequency, discontinuous reflectors around site M0079 is consistent with such a down-dip flow evolution from relatively high- to low-energy turbidity flows.

Coarse-grained sediment supply during SU-E entered from hinterland drainage catchments and the coarsest load was deposited at proximal sites and against intrabasinal structures resulting in only thin-bedded low density events reaching site M0079. The low-reflectivity character in SU-E around site M0079 thus reflects deposition and recurrence of only cm-scale graded beds and homogenous bed-types that fall below seismic resolution (Gawthorpe et al., 2022; Figure 5). We see through correlation with the lithostratigraphy of Gawthorpe et al. (2022) that SU-E is devoid of marine microfossil assemblages, except the sparse presence of shell debris, suggesting deposition of SU-E in dysoxic non-marine basinal waters during a time when the Gulf of Corinth was isolated to semi-isolated from open ocean conditions (Gawthorpe et al., 2022; McNeill et al., 2019).

5.6 | Seismic Unit F (SU-F): High-amplitude, high-frequency basin fill

5.6.1 | Observations

Seismic Unit F is bounded at the base and top by H9 and H10, and forms a southward-tilted, mildly wedge-shaped configuration in N–S dip profiles. Seismic Unit F has an overall time-thickness reaching a maximum of ca. 50 ms TWT on the southern side of the intrabasinal horst near site M0078 (Figure 7i), and converges with simple onlaps towards the Lykoporia and East-Antikyra Faults. Seismic Unit F has a time-thickness near site M0079 of ca. 40 ms TWT (Figures 4 and 6c).

Overall, SU-F is preserved as a set of elongate high-amplitude, high-frequency, continuous, parallel to sub-parallel reflector geometries (Figures 4 and 6). Proximal E–W strike profiles highlight the presence of fault-transverse, mounded reflector geometries (ca. 0.5–2 km wide and ca. 10–65 ms TWT thick), channel-levee geometries (ca. 600 m wide and ca. 30 ms TWT thick), symmetrical to asymmetrical, wave-like geometries (ca. 2 km wide and wavelengths of up to ca. 100 m) and sheet-like geometries (Table 1). Bounding the channel-levee geometries, the asymmetrical waves span up to ca. 2 km on either side (Table 1, Figure 6a). Channel-like geometries are seen to gradually flatten and transition into high-amplitude, high-frequency, continuous, parallel to sub-parallel geometries towards distal parts of the basin. Seismic Unit F corresponds to a depth range of ca. 30–55 mbsf with bedded packages that include graded bed types and homogenous mud beds (Figure 5). Oversized graded beds are particularly common within SU-F.

5.6.2 | Interpretations

Minor thickness variation in SU-F indicates syn-sedimentary fault movements (Figure 7i). Thickness variation away from the Lykoporia Fault is ascribed to activity on intrabasinal structures including the faults bounding the intrabasinal horst near site M0078. Sediment accumulation of up to ca. 50 ms TWT in proximal strike profiles points towards deposition by fault-transverse sediment transport systems (Figure 7i).

The occurrence of 'mounded' and channelized lobes within SU-F is indicative of continued sediment transport along fault-transverse channels. The close association of sediment waves (Table 1) to 'gull wing-shaped' geometries, interpreted as channel-levee geometries, supports overspill and flow-stripping processes from density-stratified flows in channels. Thinning and widening of channel-like geometries towards the distal basin floor suggest gradual loss of confinement at channel mouth transition zones. Additionally, the proximal location of geomorphological elements (Table 1), as well as correlations of SU-F to a lithostratigraphic interval with oversized graded beds (Figure 5), supports deposition by high-energy episodic turbiditic flows (Gawthorpe et al., 2022). Inactivity on intervening intrabasinal structures may have contributed to more frequent occurrences of thick-bedded events out onto the basin floor at site M0079. High reflectivity within SU-F at site M0079 could be due to this prevalence of oversized graded beds being emphasised by seismic tuning effects (Figure 5). Although oversized graded beds occur more frequently in high-to-moderate-amplitude packages, they can also be found in any reflective or opaque seismic unit.

5.7 | Seismic Unit G (SU-G): Low- to moderate-amplitude, moderate-frequency basin fill

5.7.1 | Observations

Seismic Unit G is bounded at the base and top by H10 and the seabed, respectively. Seismic Unit G is preserved as a faulted, non-uniform package with a mild wedge-shape configuration towards the Lykoporia Fault (Figure 7j). Besides the Derveni Fault, there is no demonstrable evidence of fault structures being active, including on the intrabasinal horst faults near site M0078. But this may

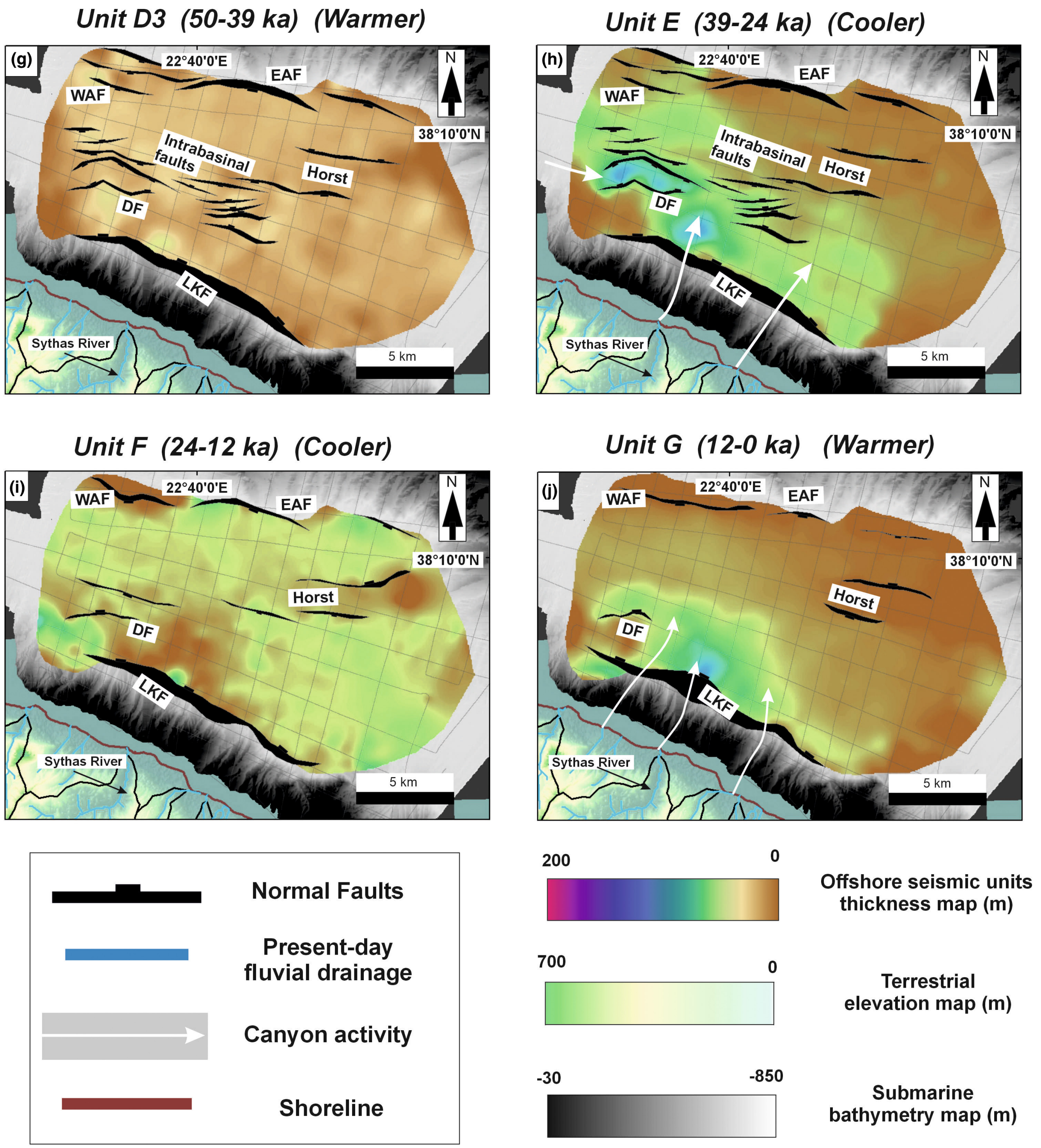

FIGURE 7 (a–j). Isopach maps (Units A–G) of the eastern Gulf of Corinth highlighting sediment dispersal patterns in alternating cooler, glacial and warmer interglacial cycles over the last ca. 242 kyr. Maps have been used as the basis for bulk volume calculations. Note the alignments of the onshore–offshore drainage networks.

reflect any continuing upward propagation of faults not having accumulated a resolvable throw on Horizon 10. Seismic Unit G is thickest in the depocentre adjacent to the Lykoporia Fault (ca. 50 ms TWT; Figures 4 and 7j). Seismic Unit G is also observed as a ca. 30 ms TWT thick unit around site M0079.

Overall, SU-G is preserved as a low- to moderate-amplitude, moderate-frequency unit (Figures 4 and 6). In proximal settings, SU-G is dominated by mounded reflector geometries (ca. 0.5–2 km wide and ca. 50 ms thick) (Figure 6a); confined channel-forms (ca. 200–400 m wide and ca. 20 ms in time-thickness); channel-levee

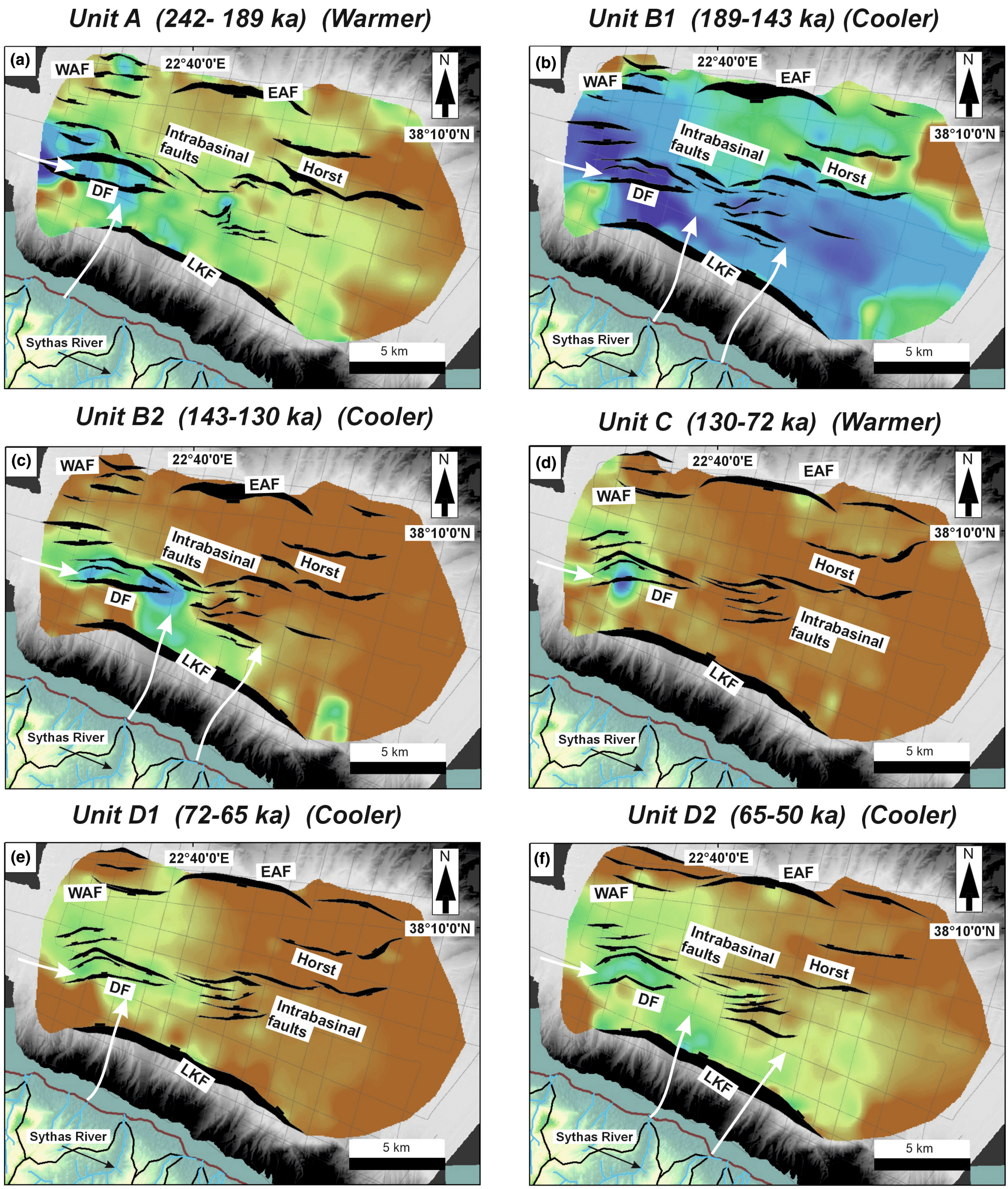

FIGURE 7 (Continued)

geometries (ca. 200–1000 m wide and ca. 20–50 ms in time-thickness) (Table 1), symmetrical to asymmetrical, wave-like geometries (ca. 2 km wide and wavelengths of up to ca. 100 m) and sheet-like geometries (Table 1). These geometries eventually flatten and thin basinward into moderate- to low-amplitude, moderate-frequency reflectors (Figure 6b,c). Seismic Unit G corresponds to a depth range of 0–30 mbsf at site M0079 and is dominantly comprised of highly bioturbated muds and is to an extent interbedded with graded bed-types (Figure 5).

5.7.2 | Interpretations

Thickness variations in proximal strike profiles, and the lack of significant activity by intrabasinal structures, suggest faulting is concentrated on the Lykoporia Fault (Figure 7j). Association of H10 with bidirectional downlaps, mounded geometries (Table 1), confined channel-forms and sheet turbidites (Table 1, Figure 6a), as well as the seabed morphology (Figure 2), supports an interpretation of SU-G as a canyon-fed submarine fan system. The presence of these geometries supports an interpretation of a sediment bypass-dominated proximal part of the basin that transitions distally to unconfined deposition (McHargue et al., 2021; Sprague et al., 2002).

The relationship of sediment waves (Table 1) to 'gull-wing shaped' channel-levee geometries implies overspill and flow striping of turbidity currents as the formative mechanism of these seismic geometries. Shallowing and widening of channel-like geometries towards the distal basin floor suggests gradual loss of confinement via channel mouth transition zones. The geomorphological elements and variations in thickness in the hanging wall of the Lykoporia Fault indicate the presence of several bases of slope fan systems in SU-G (Table 1, Figure 6a). Correlations of SU-G to bioturbated bed-types, interbedded with oversized graded-beds and homogenous muds at M0079 (Gawthorpe et al., 2022) imply deposition at the site was largely from turbidity underflows or lofted plumes. Moderate reflectivity within SU-G is interpreted to be due to the occurrence of the oversized graded beds (Figure 5).

6 | TEMPORAL SEDIMENT DISPERSAL PATTERNS OVER THE LAST CA. 242 KYR

Mapped seismic units and horizons have been validated and calibrated using IODP wells M0078 and M0079. Seismic Unit A is the oldest unit, with H1 dated as ca. 242 ka and H2 at ca. 189 ka. Seismic Unit A is a moderate- to high-amplitude, moderate-frequency package, deposited during a phase of distinct climate variability associated with the interglacial (MIS 7) period. This corresponds to a period of sea-level rise and highstand, which produced the change in basin conditions from an isolated to semi-isolated basin to an open marine basin (Gawthorpe et al., 2022; McNeill et al., 2019). Sediment volumes on the isopach map are interpreted as submarine fans active during the MIS 7 interglacial highstand (Figure 7a), with the Sythas canyon and potentially an axial input from the west supplying the basin floor (Figure 7a). During this period, nearly all transverse canyon systems, except for one, were effectively deactivated, and depocentres lacked adequate connectivity to their source. In addition, axial flow-related pathways in the hanging wall of the Derveni Fault may have been active, potentially due to the influence of the Krathis River (Watkins et al., 2018). These pathways seem to have been capturing lateral input from the southern margin between the Krathis River and Derveni (Watkins et al., 2018). The Sythas shelf-indenting canyon which was active at this time is aligned to a fluvial network and could also have captured sediments from adjacent sediment distribution networks if some sediments were supplied to the canyon head via longshore drift (Covault et al., 2007; Sweet et al., 2020).

Seismic Unit B is a low-amplitude package with thick discontinuous reflectors along dip profiles. Correlations to borehole M0079 (Gawthorpe et al., 2022) support the base of SU-B (Horizon 2) being at the onset of MIS 6. H3, interpreted as a lithostratigraphic tie point at ca. 143 ka, subdivides SU-B into SU-B1 and SU-B2 but does not correlate to paleoenvironmental or MIS tie-points. The IODP lithofacies correlation also shows a lack of distinct change from SU-B1 to SU-B2. Lithostratigraphic tie-points from borehole M0079 place deposition of SU-B during a glacial, low sea-level period. Sediment accumulation and the presence of multiple coeval sediment transport systems supplying the basin floor are recognised on the isopach maps, which are interpreted to represent submarine fan deposits during the MIS 6 glacial lowstand from ca. 189 to 130 ka (Figure 7b,c). We interpret shoreline regression with fluvial systems extending across the narrow shelf would have facilitated basinward sediment supply and submarine fan deposition during a glacial period of low sea-level. An axial sediment pathway may be present in SU-B, particularly SU-B2, with areas of sediment accumulation along the Derveni Fault; we therefore speculate that additional sources are located westward of the study area (Watkins et al., 2018; Figure 7b,c). Localisation of faults from ca. 242 ka led to the initiation and emergence of intrabasinal structures as a key component in routeing or trapping sediments towards the east (Figure 7b,c).

The overlying high-amplitude, undulating H4 is calibrated by a lithostratigraphic tie point at ca. 130 ka, which supports the start of SU-C deposition being at the onset of MIS 5e (i.e. during the MIS 6 to MIS 5 deglacial transgression). The overlying SU-C is interpreted to have formed during a period of base level rise and relative highstand. The transition from low-amplitude SU-B to high-amplitude SU-C packages, recognised by previous authors (Nixon et al., 2016; Watkins et al., 2018), is interpreted to correlate with this period of marine incursion. The seismic response of SU-C is linked to the prevalence of stratified oversized graded beds (Figure 5) composed of coarser-grained sediments that were thick enough, frequent enough and sufficiently undisturbed by bioturbation to contribute to reflectivity.

We interpret the deposition of SU-C to have spanned from ca. 130 to 72 ka, from MIS 5e to MIS 5a (Figure 7d). Seismic Unit C has a distinctive seismic character, particularly along areas adjacent to border faults, represented by a repetition of high-amplitude, high-frequency intervals with an intervening low-amplitude, low-frequency and opaque package (Figures 4a–d and 5). We interpret SU-C to represent a period of distinct climatic variability associated with MIS 5 stadials and interstadials (5a–e). MIS 5 saw little to no submarine fan deposits at the toe of the Sythas canyon. Growth of the Derveni Fault and intrabasinal structures might have allowed any local eastward axial routing to become more significant during the MIS 5 period (Figure 7d).

The top of MIS 5 is H5, which has an age-tie of ca. 72 ka. This boundary represents a period of distinct climatic change associated with SU-D, signifying basin transition from an open to an isolated or semi-isolated basin. We interpret H5 at ca. 72 ka to represent a period associated with the MIS 5a to MIS 4 transition. Seismic Unit D (which is made up of SU-D1 to SU-D3) is picked as H5 at its base and H8 at the top. These horizons have age-ties of ca. 72 and 39 ka, respectively. Seismic Unit D represents a period corresponding to the MIS 4 glacial lowstand and the MIS 3 transitional interglacial stage, the latter approximated by SU-D3 (Figure 3). H6 and H7, dated at ca. 65 and 50 ka respectively, split the moderately-reflective Seismic Unit D into SU-D1, SU-D2 and SU-D3. (Figure 5). Vertically nested architectural elements are bounded by undulating surfaces that correspond to a shift in stratal stacking pattern during SU-D (Figure 6a).

Drawing from ties to borehole M0079 (Gawthorpe et al., 2022; Maffione & Herrero-Bervera, 2022; McNeill et al., 2019) and the revised age model (after Maffione & Herrero-Bervera, 2022), there is a good correlation of a transition between laminated and bedded packages to an age-tie at ca. 39 ka during the mid to late MIS 3 global highstand. Sea-level, however, was low relative to other interglacials (MIS 7, 5 and 1) and there is not a strong signal of marine conditions within the basin at this time.

The SU-E isopach map highlights that this period (ca. 39–24 ka) was dominated by stacked submarine channel-belts in proximal settings, encompassing a period where active sediment transport systems extended towards the basin, thus maintaining a connection to terrestrial sediment sources (Figure 7h).

The onset of SU-F deposition, marked by H9, corresponds to an age-tie at ca. 24 ka during MIS 2 (Figure 5). The isopach map for this interval (Figure 7i) suggests the detachment of all sediment transport systems from sediment sources during this interval from ca. 24 to 12 ka. However, occurrences of channelized lobes within SU-F are indicative of continued sediment transport along fault-transverse channels, including the Sythas canyon (Figures 4 and 7i).

Paleoenvironmental proxies and age-depth series suggest that H10 represents the transition into the Holocene interglacial (SU-G) period at ca. 11.7 ka. The interval encompasses an extensively bioturbated, mud-dominated interval (Figure 5). The isopach map highlights a large radial-shaped fan system deposited exclusively at the base of the Sythas canyon (Figure 7j). Unlike previous interglacial highstands, the bulk of Holocene canyons, except for three, were reactivated as major sediment conduits (Figure 7j).

7 | SEDIMENT FLUX OVER THE LAST CA. 242 KYR

The average sediment flux in the eastern Gulf of Corinth over the last ca. 242 kyr is $0.276 \pm 0.01\,km^3/kyr$. Sediment flux was ca. 2 times higher during glacials (average with a standard error: $0.308 \pm 0.025\,km^3/kyr$) than interglacials (average with a standard error: $0.178 \pm 0.09\,km^3/kyr$) (Table 2, Figure 8a). Excluding the Holocene, these rates are ca. 4 times higher during glacials (average with a standard error: $0.308 \pm 0.025\,km^3/kyr$) than during interglacials (average with a standard error: $0.08 \pm 0.03\,km^3/kyr$). The Holocene (SU-G) is a striking exception, with sediment flux ca. 5 times higher ($0.374 \pm 0.03\,km^3/kyr$) than other interglacials (MIS 5 and 7) ($0.08 \pm 0.03\,km^3/kyr$). The sequential isopach maps indicate that during the pre-Holocene highstands, the termination of most basin-transverse sediment transport systems, and low sediment export to the deep-basin, can explain the low sediment flux during interglacials (Figure 7a,d,g). Units deposited during glacial periods (SU-B [MIS 6], SU-D1 and SU-D2 [MIS4] and SU-E and SU-F [MIS2]) have much higher sediment flux (maximum: $0.453\,km^3/kyr$, minimum: $0.257\,km^3/kyr$ and average: $0.308 \pm 0.025\,km^3/kyr$; Table 2). Isopach maps highlight increased export by transverse point sources, contributing to the high sediment flux during these glacials (Figure 7b,c,e,f,h,i). In contrast, the Holocene interglacial (SU-G) high sediment flux reflects the reactivation of most transverse transport systems contributing to its anomalously high sediment flux.

8 | DISCUSSION

8.1 | Impact of Late-Pleistocene glacial–interglacial climatic variability on sediment flux and fan deposition

Sediment was supplied to the eastern Gulf of Corinth via multiple transverse canyons that incised the submarine footwalls of the southern-margin border faults, forming overlapping fan morphologies during glacial periods and

TABLE 2 Calculated sediment volumes, estimated duration of deposition and sediment flux rates for all interpreted seismic units and sub-units (rates also shown in Figure 8a).

Seismic units	Approx. MIS stage	Area (km^2)	Duration (T) (k.y)	Bulk volume (V) (m^3)	Sediment volume (V_s) (km^3)	Sediment flux (R) (km^3/k.y)
Unit G	MIS 1 (interglacial)	2.43E+08	12	8.89E+09	4.49	0.374
Unit F	MIS 2 (glacial)	2.35E+08	12	1.09E+10	5.43	0.453
Unit E	MIS 2 and 3 (glacial)	2.35E+08	15	8.70E+09	4.35	0.29
Unit D3	MIS 3 (interstadial)	2.33E+08	11	3.69E+09	1.85	0.168
Unit D2	MIS 3 and 4 (glacial)	2.28E+08	15	9.12E+09	4.56	0.304
Unit D1	MIS 4 (glacial)	2.29E+08	7	6.30E+09	3.15	0.45
Unit C	MIS 5 (interglacial)	2.25E+08	58	6.72E+09	2.89	0.05
Unit B2	MIS 6 (glacial)	2.23E+08	13	7.73E+09	4.02	0.309
Unit B1	MIS 6 (glacial)	2.21E+08	46	2.27E+10	11.83	0.257
Unit A	MIS 7 (interglacial)	2.25E+08	53	1.12E+10	5.82	0.11

at low sea levels (MIS 2, 4 and 6) (Figure 9). The fault-controlled slopes, river-canyon connectivity and negligible shelf storage link sediment flux from the rivers to the deep basin at these times. In contrast, during interglacial conditions, most canyons, if not all, are interpreted as inactive, except during the Holocene (SU-G) (Figures 7 and 9). During glacials, such as MIS 2, 4 and 6, unlike during interglacials MIS 5 and 7, the connectivity between active sediment transport systems and adjacent depocentres becomes apparent. This is evident in the thicknesses observed along the depocentres and the development of submarine fan systems (Figure 7). Inactive systems, however, exhibit relatively poor connectivity during interglacials of MIS 5 and 7, resulting in reduced or intermittent sediment supply, leading to diminished or stalled sediment deposition in adjacent areas (Figures 7 and 9).

Furthermore, our results identify links between basinal sediment flux and climate change (Table 2, Figure 8). When combined with palynological data, the results show that periods of distinct vegetation reorganisation correlate with sediment flux variations. Interglacial periods show increases in Mediterranean tree taxa, whilst these trees do survive glacial periods in the Corinth catchments but at lower percentages of the total tree pollens (Figure 8c). During glacial periods, steppe vegetation assemblages peak (Kafetzidou et al., 2023). This vegetation record contrasts with a more marked alternation between assemblages dominated by arboreal pollens during interglacials versus assemblages dominated by non-arboreal steppic flora (NAP) during glacials, as exemplified by the Tenaghi Philippon record in northern Greece, summarised in Figure 8d (Koutsodendris et al., 2023; Milner et al., 2016; Pross et al., 2015; Tzedakis et al., 2006) and by Lake Ioannina (Lawson et al., 2004; Roucoux et al., 2011; Tzedakis, 1994) records.

Our results demonstrate a tendency for increased sediment flux during the colder glacial periods to the Corinth Rift sink (MIS 2, 4 and 6). This increase can be primarily attributed to glacial climatic conditions with a combination of lower temperatures and/or lower moisture availability, leading to a greater proportion of mixed forest and herbaceous vegetation at a time of reduced tree cover (Kafetzidou et al., 2023). We see that this partially deforested landscape leads to an increase in the yield of 'soft' sediments from lowland and/or upland regions, such as soils and reworked trapped sediments, during periods of sea-level or base-level fall (Cullen et al., 2021; Leeder et al., 1998). Elevated sediment flux may also reflect the presence of easily erodible sediments that are partially exposed on the narrow shelf during lowstands (McNeill et al., 2019). In addition, Gawthorpe et al. (2022) reported an increased proportion of graded beds (by thickness) in laminated and bedded packages deposited in the Gulf of Corinth during glacial periods compared to bioturbated packages deposited during interglacial periods, supporting the suggestion that maximum deposition occurred during cooler glacial conditions. We propose that a relative increase in steppe vegetation compared to arboreal taxa can result in stadial–interstadial timescale alterations in erosion patterns and sediment budgets, despite the preservation of Mediterranean and Mesophilous trees during glacials in lower altitude refugia (Kafetzidou et al., 2023).

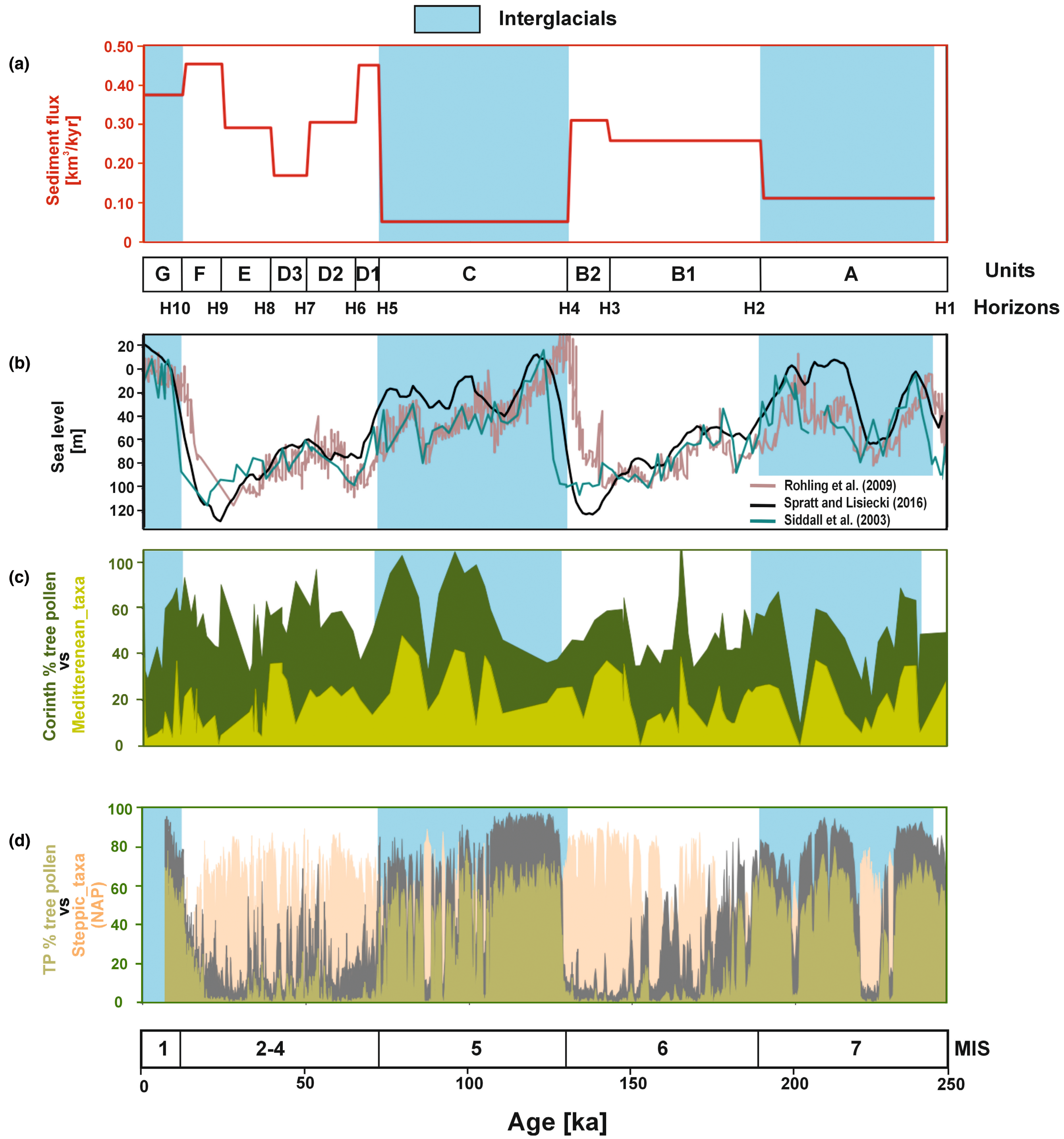

FIGURE 8 Summary of sediment flux rates combined with sea-level and palynology records over the last ca. 242 kyr. (a) Sediment flux rates from defined seismic units in km^3/kyr (red) from (Table 2) correlated to (b) (Rohling et al., 2009; Siddall et al., 2003; Spratt & Lisiecki, 2016) relative sea-level curves and (c) (Kafetzidou et al., 2023) high-resolution palynology showing percentage of total tree pollen (dark green) and Mediterranean tree taxa (yellow green) for the Gulf of Corinth and (d) highlights total AP (green + grey) vs. total NAP (peach) abundances for the TP (Tenaghi-Philippon) site in northern Greece (Koutsodendris et al., 2023). Cyclicity in sediment flux rates for the last ca. 242 kyr is proposed to reflect distinct periods of climatic variability.

The differing activity levels between the Sythas and adjacent transport systems could be attributed to variations in sediment production and discharges, which are likely higher in the larger terrestrial Sythas drainage compared to adjacent juvenile drainage networks during interglacials (Figures 1 and 9; Leeder et al., 1998). This corresponds with global studies by Nyberg et al. (2018) which emphasise that larger catchments generally generate

Basin Research IAS EAGE —WILEY

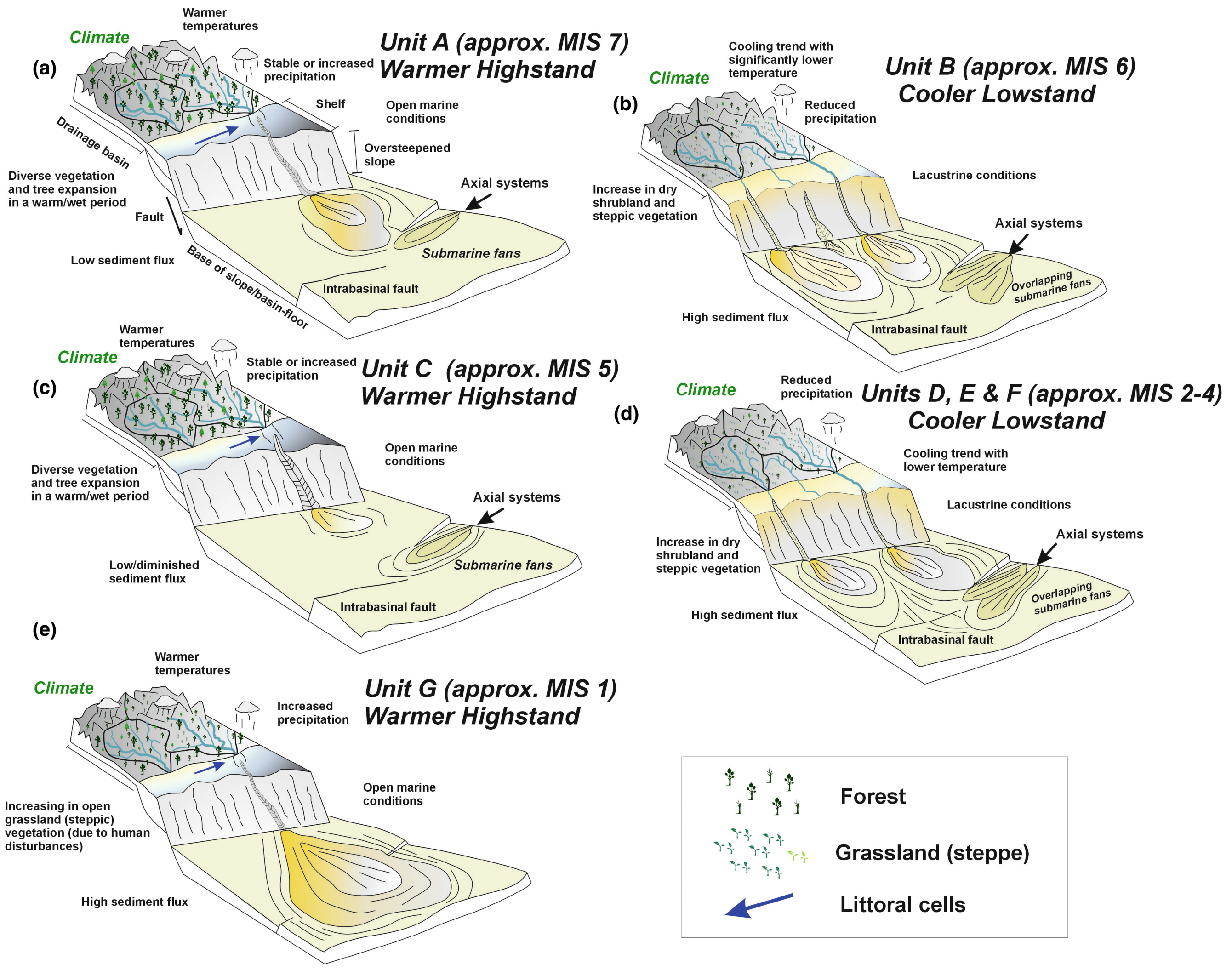

FIGURE 9 Simplified diagram of the evolution of the depositional system and sediment dispersal patterns in the last ca. 242 kyr from (a) Marine Isotope (MIS) 7, through (b) MIS 6, (c) MIS 5, (d) MIS 2–4 to (e) MIS 1.

and discharge more sediment than smaller catchments over extended periods, albeit in a database of much larger catchments than those in this case study. During the glacial period, it is anticipated that the Corinth Rift experienced a decrease in temperature and vegetation cover (Kafetzidou et al., 2023). These alterations are expected to result in increased physical weathering (Tucker et al., 2011), sediment production (Hales & Roering, 2007) and periglacial processes (Font et al., 2006; Lundberg & McFarlane, 2007), particularly due to increases in freeze–thaw weathering. Consequently, these conditions are likely to foster heightened sediment generation and transfer (Leeder et al., 1998). These shifts are apparent as all contemporary sediment transport systems have been activated, possibly due to increased activity in both large and small terrestrial drainage systems, leading to the transportation of sediments to adjacent depocentres and submarine fan systems (Figure 9; Heckmann et al., 2018; Normandeau et al., 2017). The Sythas canyon sustained sediment supply to the deep sea during both glacial and interglacial periods (Table 2, Figure 9). Therefore, the Sythas Canyon is not sensitive to cyclic sea level changes (Figures 8 and 9). This demonstrates that the basin configuration with its narrow shelf can produce scenarios in which deep-sea deposition occurs at all sea-level stands.

Higher sediment flux during the cooler glacial periods in this study and others (Collier et al., 2000; McNeill et al., 2019) contrast with the conclusions of Watkins et al. (2018), who calculated higher sediment flux during interglacials. Most horizons used here and in Watkins et al. (2018) are similar (Figure 3). However, discrepancies in sediment flux between our study and Watkins et al. (2018) can be attributed to differences in interpreted horizons for MIS 5 and the time duration assigned for glacial periods. Extending their Unit II to 100 ka as assigned by Watkins et al. (2018), instead of 72 ka, results in underestimated sediment fluxes during glacial periods and overestimation of sediment fluxes during interglacial periods. Watkins et al. (2018) reported a sediment flux of 0.91 km^3/kyr for their Unit II (MIS 2–4; 12–100 ka), whereas our data indicate a sediment flux of 1.67 km^3/kyr for SU-B, D and E (MIS 2–4; 12–72 ka). When the MIS 2–4 (referred to as Unit II in Watkins et al., 2018) is correlated with the 72–12-ka period used in our study, a higher sediment flux of 1.33 km^3/kyr is found, exceeding the sediment flux of 0.58 km^3/kyr calculated for the interglacial interval (which they interpreted as their Unit III). Unlike Watkins et al. (2018), who calculated sediment flux for the entire basin, our analysis, focused on the eastern Gulf of Corinth, offers insights into sediment flux variations across the enclosed clastic sink, akin to the approach of Collier et al. (2000) in the Gulf of Alkyonides.

In our review, peaks in sediment flux correspond to glacial periods. The difference in sediment flux between studies is attributed to the recent acquisition of higher-resolution datasets, comprising a detailed chronological framework (Gawthorpe et al., 2022; Maffione & Herrero-Bervera, 2022; McNeill et al., 2019), an integrated age-depth model (Maffione & Herrero-Bervera, 2022) and a robust velocity model based on the IODP 381 boreholes, which were not available in previous studies. Furthermore, this is the first study of sediment flux derived from volumes based on mapping seismic horizons over timescales of stadials and interstadials (10^4) cycles tied to the IODP Expedition 381 boreholes.

In examining the impact of precipitation on the system, it has been proposed that mean annual precipitation did not change significantly between glacial and interglacial conditions (Watkins et al., 2018). The relationship between precipitation extremes and temperature has been widely discussed in the scientific literature (e.g., Berg et al., 2013; Drobinski et al., 2018; Xoplaki et al., 2004). It is accepted that glacial periods tend to exhibit greater variability, seasonality and storminess in precipitation compared to interglacial periods (Drobinski et al., 2018; Kafetzidou et al., 2023; Kolodny et al., 2005; McNeill et al., 2019; Pennos et al., 2022). However, the evolution of extreme precipitation events in the Gulf of Corinth remains unclear. In light of this, we hypothesise that cyclic variations in runoff could result in highly punctuated erosion rates, with sediment mobilisation concentrated during glacial periods of increasing runoff variability and/or decreasing vegetation cover (Ott, 2020; Pennos et al., 2022).

It is unlikely that variations in fault activity (slip rates) were responsible for the cyclicity of sediment discharge during the Late Quaternary. Any tectonic impacts operating on 10^5–10^6 timescales in this basin during the studied interval seem to be of lower magnitude than the climatic variation caused by the glacial–interglacial cycles (Nixon et al., 2016). The temporal correlation of sediment flux to palynology in the Gulf of Corinth is evidence that variability of sediment flux is largely governed by climate-related changes affecting adjacent hinterland catchments, with sea-level and tectonics being second-order controls on these time scales.

8.2 | Holocene climate variability and its effect on sediment flux

The sediment flux during the Holocene was ca. 5 times higher than the average for the earlier interglacial periods (Figure 8, Table 2). We propose that two factors may have contributed to this anomaly: climate and anthropogenic activity.

High-resolution records of isotopes from caves and lakes provide evidence for an increase in precipitation in the north-eastern Mediterranean and the Levant region from ca. 9.5 to 6.5 ka (Bar-Matthews & Ayalon, 2011; Joannin et al., 2013; Parton et al., 2018; Regattieri et al., 2023; Spötl et al., 2010). Global climatic data (e.g. Hijmans et al., 2005; Watkins et al., 2018 and references therein) and sedimentological analyses from other locations in the Mediterranean also support a pluvial episode during the early to mid-Holocene (Pennos et al., 2022; Roberts et al., 2019; Stamatis et al., 2022). However, pollen-based reconstructions indicate that the mid-Holocene (9–7 ka) was interrupted by arid phases (Kyrikou et al., 2020; Lacey et al., 2015; Roberts et al., 2019) and reveal contrasting climatic trends in the mid-Holocene climatic transition (8–6 ka) in the Mediterranean, indicating precipitation variability across the Mediterranean (as noted in both lacustrine and marine records) (Hou et al., 2023; Kotthoff et al., 2008; Magny et al., 2013; Roberts et al., 2001). Moreover, several studies (Cai et al., 2023; Lacey et al., 2015; Wei et al., 2021) have indicated that the Holocene pluvial climate in the Mediterranean region differed from the Marine Isotope Stage 5 (MIS 5) interglacials in terms of temperature stability, precipitation variability and vegetation density. During the Holocene, the climate was characterised as relatively stable and warm conditions though precipitation varied to some extent (Ott, 2020). In contrast, the MIS 5 interglacials experienced greater temperature fluctuations and higher precipitation variability, with colder and drier stadials alternating with warmer and wetter interglacials and interstadials (Milner et al., 2013; Ott, 2020). Consequently, we hypothesise that the prolonged and stable conditions of the Holocene pluvial period allowed for more continuous and substantial sediment transport in the Mediterranean compared to the more variable interglacials MIS 5 and 7.

Climatic changes may have been sufficient to promote sediment supply across the narrow Gulf of Corinth footwall shelf, even during periods of sea-level rise.

Fuchs (2007) and McNeill et al. (2019) conclude that temperature and precipitation alone cannot explain increased sediment flux during the Holocene interglacial period. The mid-late Holocene is proposed to have witnessed significant ecological changes in the Gulf of Corinth marked by low arboreal pollen (AP) concentrations and an increase in herbaceous plants such as the Cichorieae and Chenopodiaceae that were less directly related to climate (Kaniewski et al., 2007; Lawson et al., 2004).

The second potential explanation is anthropogenic disturbance. Neolithic (ca. 8–4 ka) occupations may have contributed to enhanced erosion due to forest clearances and agriculture. A deforested landscape has limited capability to control erosion (Corenblit et al., 2009) and the ability of runoff to dislodge sediment is enhanced, ultimately leading to the mobilisation of softer sediments (Leeder et al., 1998; Turnbull et al., 2009). Such phenomena are observed throughout the Peloponnese (Butzer, 2005), Anatolia (Hodder, 2014; Roberts et al., 2019) and Iberia (Pérez-Lambán et al., 2018). Mediterranean geoarchaeological (Stamatopoulos et al., 2019) and pedological (Fuchs, 2007; Pérez-Lambán et al., 2018) records suggest that human-induced vegetation change since the 7th millennium BCE (ca. 8.5 ka) may have played a role in sediment redistribution. The correlation between sedimentation rates and catchment development for proto-agricultural use indicates that sedimentation rates increased at the onset of the Neolithic period (at ca. 8 ka) (Fuchs, 2007; Roberts et al., 2019). Colluvial records from the Chalcolithic and Middle Bronze Age (ca. 4.5–3.5 ka) in NE Peloponnesos (Fuchs, 2007) and elsewhere in Greece (Haenssler et al., 2013; Kyrikou et al., 2020) also demonstrate that sedimentation rates decreased considerably when human-disturbances became less intensive, implying that erosion rates can be reversed. Based on these findings, it is probable that erosion during the Holocene would have been lower in the absence of human activity.

Previous interglacials have been documented to exhibit climate changes, whether changes in temperature, precipitation and/or seasonality (e.g. Milner et al., 2013). However, we contend that climate alone is insufficient to account for the increased sediment flux observed during the Holocene, especially when considering that other climatic shifts (during MIS 5 and 7) did not lead to the same responses (Figure 8). Therefore, human activity likely contributed to the anomalously high sediment flux documented during the Holocene.

8.3 | Hierarchy of controls in deep-water systems

Our study has allowed an overall evaluation of the depositional sink in the eastern Gulf of Corinth. Interactions of various source-to-sink parameters, such as tectonics, climate, hinterland characteristics and autogenic factors, play a role in shaping sediment supply changes (Allen, 2008b; Romans et al., 2016; Sømme et al., 2009). On 10^6 year time scales, regional-scale factors, such as active tectonics in the Gulf of Corinth, have played a crucial role in shaping and developing basin bounding structures and influencing canyon characteristics (Barrett et al., 2019; Sakellariou et al., 2007; Taylor et al., 2011). These factors impact the positioning, width and ultimately the gradient, of canyons developed on major subaqueous fault scarps, exerting control over the positioning of base-of-slope fan systems and the basin floor sediment transport system. Intrabasinal structures also influence transport pathways for sediment routeing across the basin floor and influence the thickness of sediment accumulations through local accommodation variation (Bell et al., 2009; Nixon et al., 2016).

Factors of regional spatial scale and 10^4–10^5 year timescales include climatic changes, which have a notable impact on the cyclical patterns observed in the basin fill (Collier et al., 2000; Maffione & Herrero-Bervera, 2022; McNeill et al., 2019). The narrowness, or the absence, of a shelf in the eastern Gulf of Corinth enhances the sensitivity of the region to repeated peaks in sediment transfer at the 10^4 year timescale, as documented in this study and elsewhere (Carvajal & Steel, 2006; Picot et al., 2016; Romans et al., 2016; Savoye et al., 2009) (Figures 2, 7 and 9). Sweet and Blum (2016) have suggested that during sea-level highstands, the proximity of canyon heads to adjacent hinterland catchments allows sediment supply to be maintained to base-of-slope fans. In contrast, this study demonstrates that only some canyons directly fed by rivers may continue to supply sediments to base-of-slope fans when there is a concurrent decrease in run-off or decrease in the seasonality of precipitation during interglacial episodes.

At 10^4–10^5 timescales, we also find that adjacent hinterland catchments, may shift fan systems between active and non-active phases (Sømme et al., 2009). Steady fluvial-canyon discharges, as is common in large hinterland catchments (e.g. as discussed by Sømme et al., 2009 and references therein), along with increased sediment input resulting from specific climatic conditions, play a role in determining the activity of submarine fans over time. As a product of the short and sharp source-to-sink configuration, the Sythas base-of-slope fan system is linked to the behaviour of onshore catchments as seen throughout the Late Quaternary despite adjustment to these relations by changes in tectonics and climate (Collier et al., 2000; Cullen et al., 2021; Gawthorpe et al., 2018; Leeder et al., 1998; McNeill et al., 2019; Pechlivanidou et al., 2019).

On a 10^3–10^4 year timescale, autogenic processes, such as sediment storage and release, can have a notable impact on sediment flux dynamics (Allen, 2008a; Kim et al., 2006). These processes are influenced by various factors, including sediment supply and changes in shoreline discharge (Straub et al., 2015; Wang et al., 2011). Autogenic sediment transport changes can arise from intermittent sediment accumulation and/or accelerated transport within the transfer zone, for example, triggered by transient landforms and human-induced alterations to vegetation. The role of autogenic processes highlights the challenge of linking specific signals of external forcing to sediment fluxes or volumes. However, with more core data, a hydraulic grain-size approach (Tofelde et al., 2021) might help to reveal the signals of short-term perturbations experienced in the drainage basins preserved within deep-water successions. Nonetheless, this study demonstrates that deep-water systems can be treated as reliable archives of the sedimentary responses to environmental change on glacial–interglacial timescales.

9 | CONCLUSIONS

Integration of multiple datasets and high temporal resolution stratigraphic constraints from IODP Expedition 381 enables the assessment of sediment flux over the past ca. 250 kyr in the eastern Gulf of Corinth, including between time-slices of approximately every 10^4 years since MIS 5.

1. Results indicate a link between sediment flux and alternating cooler (glacial; MIS 2, 4 and 6) and warmer (interglacial; MIS 5 and 7) climatic cycles, including stadial–interstadial cycles.
2. Sediment flux was twice as high during cooler glacial periods compared to warmer interglacial periods (MIS 7 and 5), but with the Holocene interglacial (MIS 1) exhibiting five times greater sediment flux than the previous two interglacial cycles (MIS 5 and 7).
3. Lower sediment flux coincides with interglacials having higher abundances of Mediterranean trees. Higher sediment flux correlates with glacials (MIS 2, 4 and 6) featuring reduced Mediterranean taxa derived from Corinth Rift catchments. High sediment fluxes during the Holocene likely reflect significant anthropogenic influence, such as Neolithic occupations, deforestation and agriculture, which enhanced erosion and limited landscape erosion control.
4. Sediment supply results from changes in the activity versus inactivity of multiple transverse transport systems and their connectivity to the immediate hanging wall of the southern-margin border faults. Differences in basinward sediment transfer between the Sythas and adjacent transport systems reflect variable connectivity between rivers and canyons during glacial and interglacial periods. All canyons exhibit increased activity during glacials, providing heightened sensitivity to onshore signals in basinal records.
5. Increases in sediment flux during cooler (glacial) conditions indicate higher erosion rates and discharge, representing the most reliable signal from the erosional part of the catchments. Increased sediment transport from terrestrial drainages to adjacent depocentres and submarine fan systems thus highlights the dynamic nature of linked onshore–offshore sediment transport systems.
6. The physiographic configuration of the Sythas canyon-incised system, with a narrow shelf and steep slope, leads to low sensitivity to sea level, allowing deposition at any point on the sea-level curve.
7. This study demonstrates the value of deep-water systems in rift basins as important archives for recording sedimentary responses to environmental change.

ACKNOWLEDGEMENTS

This work forms part of the PhD thesis of Mohamed A. Mohamed (MAM). The DeepRift project, hosted at the University of Bergen, and funded by the Research Council of Norway (Project Number 308805) financed data acquisition and partially funded MAM's PhD. The LOBE 3 consortium project also partially funded MAM's PhD, and we are grateful for the support from Aker BP, BHP, BP, Equinor, HESS, Neptune, Petrobras, PetroChina, Total, Var Energi and Woodside. The authors extend gratitude to the Hellenic Centre of Marine Research for the acquisition of bathymetry and seismic reflection data using the R/V Aegaeo in the Gulf of Corinth, and the processing of these data. In addition, we would like to convey our thanks to Casey Nixon and Marco Maffione for discussions on IODP Expedition 381 data. We thank the reviewers Ivar Midtkandal, Miguel Garces, and Sébastian Rohais, and Editor Cari Johnson, for their careful, constructive, and thorough reviews of this manuscript. Their valuable feedback has greatly improved the quality of this work.

DATA AVAILABILITY STATEMENT

The data supporting the findings of this study can be obtained on request from the authors.

ORCID

Mohamed A. Mohamed https://orcid.org/0000-0002-7121-1564
David M. Hodgson https://orcid.org/0000-0003-3711-635X

Rob L. Gawthorpe https://orcid.org/0000-0002-4352-6366
Donna J. Shillington https://orcid.org/0000-0003-1058-3871
Martin Muravchik https://orcid.org/0000-0002-1330-0673

REFERENCES

Adeogba, A. A., McHargue, T. R., & Graham, S. A. (2005). Transient fan architecture and depositional controls from near-surface 3-D seismic data, Niger Delta continental slope. *American Association of Petroleum GeMayallologists Bulletin*, *89*(5), 627–643. https://doi.org/10.1306/11200404025

Allen, P. A. (2008a). From landscapes into geological history. *Nature*, *451*(7176), 274–276. https://doi.org/10.1038/nature06586

Allen, P. A. (2008b). Time scales of tectonic landscapes and their sediment routing systems. *Geological Society Special Publication*, *296*, 7–28. https://doi.org/10.1144/SP296.2

Armijo, R., Meyer, B. G., King, G. C., Rigo, A., & Papanastassiou, D. (1996). Quaternary evolution of the Corinth Rift and its implications for the Late Cenozoic evolution of the Aegean. *Geophysical Journal International*, *126*, 11–53.

Bakke, K., Kane, I. A., Martinsen, O. J., Petersen, S. A., Johansen, T. A., Hustoft, S., Jacobsen, F. H., & Groth, A. (2013). Seismic modeling in the analysis of deep-water sandstone termination styles. *AAPG Bulletin*, *97*(9), 1395–1419. https://doi.org/10.1306/03041312069

Bar-Matthews, M., & Ayalon, A. (2011). Mid-Holocene climate variations revealed by high-resolution speleothem records from Soreq cave, Israel and their correlation with cultural changes. *The Holocene*, *21*(1), 163–171. https://doi.org/10.1177/0959683610384165

Barrett, B. J., Collier, R. E. L. L., Hodgson, D. M., Gawthorpe, R. L., Dorrell, R. M., & Cullen, T. M. (2019). Quantifying faulting and base level controls on syn-rift sedimentation using stratigraphic architectures of coeval, adjacent early-middle Pleistocene fan deltas in Lake Corinth, Greece. *Basin Research*, *31*(6), 1040–1065. https://doi.org/10.1111/bre.12356

Beaubouef, R. T. (2004). Deep-water leveed-channel complexes of the Cerro Toro formation, upper cretaceous, southern Chile. *AAPG Bulletin*, *88*(11), 1471–1500. https://doi.org/10.1306/06210403130

Bell, R. E. (2008). *Tectonic evolution of the Corinth rift*. University of Southampton. http://eprints.soton.ac.uk/63290/

Bell, R. E., McNeill, L. C., Bull, J. M., Henstock, T. J., Collier, R. E. L., & Leeder, M. R. (2009). Fault architecture, basin structure and evolution of the Gulf of Corinth rift, central Greece. *Basin Research*, *21*(6), 824–855. https://doi.org/10.1111/j.1365-2117.2009.00401.x

Berg, P., Moseley, C., & Haerter, J. O. (2013). Strong increase in convective precipitation in response to higher temperatures. *Nature Geoscience*, *6*(3), 181–185. https://doi.org/10.1038/ngeo1731

Briole, P., Rigo, A., Lyon-Caen, H., Ruegg, J. C., Papazissi, K., Mitsakaki, C., Balodimou, A., Veis, G., Hatzfeld, D., & Deschamps, A. (2000). Active deformation of the Corinth rift, Greece: Results from repeated global positioning system surveys between 1990 and 1995. *Journal of Geophysical Research: Solid Earth*, *105*(B11), 25605–25625. https://doi.org/10.1029/2000JB900148

Brooks, M., & Ferentinos, G. (1984). Tectonics and sedimentation in the Gulf of Corinth and the Zakynthos and Kefallinia channels, Western Greece. *Tectonophysics*, *101*(1–2), 25–54. https://doi.org/10.1016/0040-1951(84)90040-4

Butzer, K. W. (2005). Environmental history in the Mediterranean world: Cross-disciplinary investigation of cause-and-effect for degradation and soil erosion. *Journal of Archaeological Science*, *32*(12), 1773–1800. https://doi.org/10.1016/j.jas.2005.06.001

Cai, Y., Cheng, H., Cheng, X., Shi, Z., Lu, Y., Ma, L., Pérez-Mejías, C. A., Zhang, H., Wei, Y., Xue, G., & Li, H. (2023). Orbital- to millennial-scale variation of the speleothem δ^{18}O record during marine isotope stages 5 to 3 on the southeast Chinese loess plateau and its climatic and environmental implications. *Journal of Quaternary Science*, *38*(3), 295–307. https://doi.org/10.1002/jqs.3489

Carvajal, C. R., & Steel, R. J. (2006). Thick turbidite successions from supply-dominated shelves during sea-level highstand. *Geology*, *34*(8), 665. https://doi.org/10.1130/G22505.1

Castelltort, S., & Van Den Driessche, J. (2003). How plausible are high-frequency sediment supply-driven cycles in the stratigraphic record? *Sedimentary Geology*, *157*(1–2), 3–13. https://doi.org/10.1016/S0037-0738(03)00066-6

Catuneanu, O., Abreu, V., Bhattacharya, J. P., Blum, M. D., Dalrymple, R. W., Eriksson, P. G., Fielding, C. R., Fisher, W. L., Galloway, W. E., Gibling, M. R., Giles, K. A., Holbrook, J. M., Jordan, R., Kendall, C. G. S. C., Macurda, B., Martinsen, O. J., Miall, A. D., Neal, J. E., Nummedal, D., … Winker, C. (2009). Towards the standardization of sequence stratigraphy. *Earth-Science Reviews*, *92*(1–2), 1–33. https://doi.org/10.1016/j.earscirev.2008.10.003

Clarke, P. J., Davies, R. R., England, P. C., Parsons, B., Billiris, H., Paradissis, D., Veis, G., Cross, P. A., Denys, P. H., Ashkenazi, V., Bingley, R., Kahle, H. G., Muller, M. V., & Briole, P. (1998). Crustal strain in Greece from repeated GPS measurements in the interval 1989-1997. *Geophysical Journal International*, *135*(1), 195–214. https://doi.org/10.1046/j.1365-246X.1998.00633.x

Collier, R. E. L., Leeder, M. R., Trout, M., Ferentinos, G., Lyberis, E., & Papatheodorou, G. (2000). High sediment yields and cool, wet winters: Test of last glacial paleoclimates in the northern Mediterranean. *Geology*, *28*(11), 999–1002. https://doi.org/10.1130/0091-7613(2000)28<999:HSYACW>2.0.CO;2

Corenblit, D., Steiger, J., Gurnell, A. M., Tabacchi, E., & Roques, L. (2009). Control of sediment dynamics by vegetation as a key function driving biogeomorphic succession within fluvial corridors. *Earth Surface Processes and Landforms*, *34*(13), 1790–1810. https://doi.org/10.1002/esp.1876

Covault, J. A., & Graham, S. A. (2010). Submarine fans at all sea-level stands: Tectono-morphologic and climatic controls on terrigenous sediment delivery to the deep sea. *Geology*, *38*(10), 939–942. https://doi.org/10.1130/G31081.1

Covault, J. A., Normark, W. R., Romans, B. W., & Graham, S. A. (2007). Highstand fans in the California borderland: The overlooked deep-water depositional systems. *Geology*, *35*(9), 783–786. https://doi.org/10.1130/G23800A.1

Cullen, T. M., Collier, R. E. L., Gawthorpe, R. L., Hodgson, D. M., & Barrett, B. J. (2020). Axial and transverse deep-water sediment supply to syn-rift fault terraces: Insights from the West Xylokastro Fault Block, Gulf of Corinth. *Greece. Basin Research*, *32*(5), 1105–1139. https://doi.org/10.1111/bre.12416

Cullen, T. M., Collier, R. E. L., Hodgson, D. M., Gawthorpe, R. L., Kouli, K., Maffione, M., Kranis, H., & Eliassen, G. T. (2021).

Deep-water syn-rift stratigraphy as archives of early-mid Pleistocene Palaeoenvironmental signals and controls on sediment delivery. *Frontiers in Earth Science*, *9*, 1–32. https://doi.org/10.3389/feart.2021.715304

Deptuck, M. E., Steffens, G. S., Barton, M., & Pirmez, C. (2003). Architecture and evolution of upper fan channel-belts on the Niger Delta slope and in the Arabian Sea. *Marine and Petroleum Geology*, *20*(6-8), 649–676. https://doi.org/10.1016/j.marpetgeo.2003.01.004

Drobinski, P., Silva, N. D., Panthou, G., Bastin, S., Muller, C., Ahrens, B., Borga, M., Conte, D., Fosser, G., Giorgi, F., Güttler, I., Kotroni, V., Li, L., Morin, E., Önol, B., Quintana-Segui, P., Romera, R., & Torma, C. Z. (2018). Scaling precipitation extremes with temperature in the Mediterranean: Past climate assessment and projection in anthropogenic scenarios. *Climate Dynamics*, *51*(3), 1237–1257. https://doi.org/10.1007/s00382-016-3083-x

Elliott, G. M., Jackson, C. A. L., Gawthorpe, R. L., Wilson, P., Sharp, I. R., & Michelsen, L. (2021). Tectono-stratigraphic development of a salt-influenced rift margin: Halten terrace, offshore mid-Norway. *Basin Research*, *33*(6), 3295–3320. https://doi.org/10.1111/bre.12603

Fierens, R., Droz, L., Toucanne, S., Raisson, F., Jouet, G., Babonneau, N., Miramontes, E., Landurain, S., & Jorry, S. J. (2019). Late quaternary geomorphology and sedimentary processes in the Zambezi turbidite system (Mozambique Channel). *Geomorphology*, *334*, 1–28. https://doi.org/10.1016/j.geomorph.2019.02.033

Font, M., Lagarde, J. L., Amorese, D., Coutard, J. P., Dubois, A., Guillemet, G., Ozouf, J. C., & Vedie, E. (2006). Physical modelling of fault scarp degradation under freeze–thaw cycles. *Earth Surface Processes and Landforms*, *31*(14), 1731–1745. https://doi.org/10.1002/esp.1371

Ford, M., Hemelsdaël, R., Mancini, M., & Palyvos, N. (2017). Rift migration and lateral propagation: Evolution of normal faults and sediment-routing systems of the western Corinth rift (Greece). *Geological Society, London, Special Publications*, *439*(1), 131–168. https://doi.org/10.1144/SP439.15

Ford, M., Rohais, S., Williams, E. A., Bourlange, S., Jousselin, D., Backert, N., & Malartre, F. (2013). Tectono-sedimentary evolution of the western Corinth rift (Central Greece). *Basin Research*, *25*(1), 3–25. https://doi.org/10.1111/j.1365-2117.2012.00550.x

Fuchs, M. (2007). An assessment of human versus climatic impacts on Holocene soil erosion in NE Peloponnese, Greece. *Quaternary Research*, *67*(3), 349–356. https://doi.org/10.1016/j.yqres.2006.11.008

Gardner, M. H., Borer, J. M., Melick, J. J., Mavilla, N., Dechesne, M., & Wagerle, R. N. (2003). Stratigraphic process-response model for submarine channels and related features from studies of Permian brushy canyon outcrops, West Texas. *Marine and Petroleum Geology*, *20*(6–8), 757–787. https://doi.org/10.1016/j.marpetgeo.2003.07.004

Gawthorpe, R. L., & Leeder, M. R. (2000). Tectono-sedimentary evolution of active extensional basins. *Basin Research*, *12*(3–4), 195–218. https://doi.org/10.1111/j.1365-2117.2000.00121.x

Gawthorpe, R. L., Leeder, M. R., Kranis, H., Skourtsos, E., Andrews, J. E., Henstra, G. A., Mack, G. H., Muravchik, M., Turner, J. A., & Stamatakis, M. (2018). Tectono-sedimentary evolution of the Plio-Pleistocene Corinth rift, Greece. *Basin Research*, *30*(3), 448–479. https://doi.org/10.1111/bre.12260

Gawthorpe, R. L., Fabregas, N., Pechlivanidou, S., Ford, M., Collier, R. E. L., Carter, G. D. O., McNeill, L. C., & Shillington, D. J. (2022). Late quaternary mud-dominated, basin-floor sedimentation of the Gulf of Corinth, Greece: Implications for deep-water depositional processes and controls on syn-rift sedimentation. *Basin Research*, *34*(5), 1567–1600. https://doi.org/10.1111/bre.12671

Gee, M. J. R., Gawthorpe, R. L., Bakke, K., & Friedmann, S. J. (2007). Seismic geomorphology and evolution of submarine channels from the Angolan continental margin. *Journal of Sedimentary Research*, *77*(5), 433–446.

Haenssler, E., Nadeau, M. J., Vött, A., & Unkel, I. (2013). Natural and human induced environmental changes preserved in a Holocene sediment sequence from the Etoliko lagoon, Greece: New evidence from geochemical proxies. *Quaternary International*, *308–309*, 89–104. https://doi.org/10.1016/j.quaint.2012.06.031

Hajek, E. A., Heller, P. L., & Schur, E. L. (2012). Field test of autogenic control on alluvial stratigraphy (Ferris formation, upper cretaceous-Paleogene, Wyoming). *Geological Society of America Bulletin*, *124*(11–12), 1898–1912. https://doi.org/10.1130/B30526.1

Hales, T. C., & Roering, J. J. (2007). Climatic controls on frost cracking and implications for the evolution of bedrock landscapes. *Journal of Geophysical Research: Earth Surface*, *112*(F2), 2033. https://doi.org/10.1029/2006JF000616

Heckmann, T., Cavalli, M., Cerdan, O., Foerster, S., Javaux, M., Lode, E., Smetanová, A., Vericat, D., & Brardinoni, F. (2018). Indices of sediment connectivity: Opportunities, challenges and limitations. *Earth-Science Reviews*, *187*, 77–108. https://doi.org/10.1016/j.earscirev.2018.08.004

Heller, P. L., & Paola, C. (1992). The large-scale dynamics of grain-size variation in alluvial basins, 2: Application to syntectonic conglomerate. *Basin Research*, *4*(2), 91–102. https://doi.org/10.1111/j.1365-2117.1992.tb00146.x

Hemelsdaël, R., & Ford, M. (2016). Relay zone evolution: A history of repeated fault propagation and linkage, central Corinth rift, Greece. *Basin Research*, *28*(1), 34–56. https://doi.org/10.1111/bre.12101

Hemelsdaël, R., Ford, M., Malartre, F., & Gawthorpe, R. (2017). Interaction of an antecedent fluvial system with early normal fault growth: Implications for syn-rift stratigraphy, western Corinth rift (Greece). *Sedimentology*, *64*, 1957–1997. https://doi.org/10.1111/sed.12381

Higgs, B. (1988). Syn-sedimentary structural controls on basin deformation in the Gulf of Corinth, Greece. *Basin Research*, *1*(3), 155–165. https://doi.org/10.1111/j.1365-2117.1988.tb00012.x

Hijmans, R. J., Cameron, S. E., Parra, J. L., Jones, P. G., & Jarvis, A. (2005). Very high resolution interpolated climate surfaces for global land areas. *International Journal of Climatology*, *25*(15), 1965–1978. https://doi.org/10.1002/joc.1276

Hinderer, M. (2012). From gullies to mountain belts: A review of sediment budgets at various scales. *Sedimentary Geology*, *280*, 21–59. https://doi.org/10.1016/j.sedgeo.2012.03.009

Hodder, I. (2014). Çatalhöyük: The leopard changes its spots. A summary of recent work. *Anatolian Studies*, *64*, 1–22. https://doi.org/10.1017/S0066154614000027

Hodgson, D. M., Peakall, J., & Maier, K. L. (2022). Submarine channel mouth settings: Processes, geomorphology, and deposits. *Frontiers in Earth Science*, *10*, 790320. https://doi.org/10.3389/feart.2022.790320

Hofmann, M. H., Hendrix, M. S., Moore, J. N., & Sperazza, M. (2006). Late Pleistocene and Holocene depositional history of sediments in Flathead Lake, Montana: Evidence from high-resolution seismic reflection interpretation. *Sedimentary Geology*, *184*(1–2), 111–131. https://doi.org/10.1016/J.SEDGEO.2005.09.019

Hou, M., Wu, W., Cohen, D. J., Zeng, Z., Huang, H., Zheng, H., & Ge, Q. (2023). Detection of a mid-Holocene climate event at 7.2 ka BP based on an analysis of globally-distributed multi-proxy records. *Palaeogeography, Palaeoclimatology, Palaeoecology*, *618*, 111525. https://doi.org/10.1016/J.PALAEO.2023.111525

Janocko, M. N. W. H. S. W. M., Nemec, W., Henriksen, S., & Warchoł, M. (2013). The diversity of deep-water sinuous channel belts and slope valley-fill complexes. *Marine and Petroleum Geology*, *41*, 7–34. https://doi.org/10.1016/j.marpetgeo.2012.06.012

Jerolmack, D. J., & Paola, C. (2010). Shredding of environmental signals by sediment transport. *Geophysical Research Letters*, *37*(19), 1–5. https://doi.org/10.1029/2010GL044638

Joannin, S., Vannière, B., Galop, D., Peyron, O., Haas, J. N., Gilli, A., Chapron, E., Wirth, S. B., Anselmetti, F., Desmet, M., & Magny, M. (2013). Climate and vegetation changes during the Lateglacial and early–middle Holocene at Lake Ledro (southern Alps, Italy). *Climate of the Past*, *9*(2), 913–933. https://doi.org/10.5194/cp-9-913-2013

Jobe, Z. R., Howes, N., Romans, B. W., & Covault, J. A. (2018). Volume and recurrence of submarine-fan-building turbidity currents. *The Depositional Record*, *4*(2), 160–176. https://doi.org/10.1002/dep2.42

Kafetzidou, A., Fatourou, E., Panagiotopoulos, K., Marret, F., & Kouli, K. (2023). Unique shifts in the vegetation composition of a typical Mediterranean setting (Gulf of Corinth, Greece) during successive Quaternary climatic cycles. *Quaternary*, *6*, 30.

Kaniewski, D., de Laet, V., Paulissen, E., & Waelkens, M. (2007). Long-term effects of human impact on mountainous ecosystems, western Taurus Mountains, Turkey. *Journal of Biogeography*, *34*(11), 1975–1997. https://doi.org/10.1111/j.1365-2699.2007.01753.x

Kim, W., Paola, C., Swenson, J. B., & Voller, V. R. (2006). Shoreline response to autogenic processes of sediment storage and release in the fluvial system. *Journal of Geophysical Research: Earth Surface*, *111*(F4), F04013–F04027. https://doi.org/10.1029/2006JF000470

Kolodny, Y., Stein, M., & Machlus, M. (2005). Sea-rain-lake relation in the last glacial East Mediterranean revealed by δ^{18}O-δ^{13}C in Lake Lisan aragonites. *Geochimica et Cosmochimica Acta*, *69*(16), 4045–4060. https://doi.org/10.1016/j.gca.2004.11.022

Kotthoff, U., Müller, U. C., Pross, J., Schmiedl, G., Lawson, I. T., van de Schootbrugge, B., & Schulz, H. (2008). Lateglacial and Holocene vegetation dynamics in the Aegean region: An integrated view based on pollen data from marine and terrestrial archives. *The Holocene*, *18*(7), 1019–1032. https://doi.org/10.1177/0959683608095573

Koutsodendris, A., Dakos, V., Fletcher, W. J., Knipping, M., Kotthoff, U., Milner, A. M., Müller, U. C., Kaboth-Bahr, S., Kern, O. A., Kolb, L., Vakhrameeva, P., Wulf, S., Christanis, K., Schmiedl, G., & Pross, J. (2023). Atmospheric CO_2 forcing on Mediterranean biomes during the past 500 kyrs. *Nature Communications*, *14*, 1664. https://doi.org/10.1038/s41467-023-37388-x

Kyrikou, S., Kouli, K., Triantaphyllou, M. V., Dimiza, M. D., Gogou, A., Panagiotopoulos, I. P., Anagnostou, C., & Karageorgis, A. P. (2020). Late glacial and Holocene vegetation patterns of Attica: A high-resolution record from Elefsis Bay, southern Greece. *Quaternary International*, *545*, 28–37. https://doi.org/10.1016/j.quaint.2019.05.020

Lacey, J. H., Francke, A., Leng, M. J., Vane, C. H., & Wagner, B. (2015). A high—resolution late glacial to Holocene record of environmental change in the Mediterranean from Lake Ohrid (Macedonia/Albania). *International Journal of Earth Sciences*, *104*, 1623–1638. https://doi.org/10.1007/s00531-014-1033-6

Lawson, I., Frogley, M., Bryant, C., Preece, R., & Tzedakis, P. (2004). The Lateglacial and Holocene environmental history of the Ioannina basin, north-west Greece. *Quaternary Science Reviews*, *23*(14–15), 1599–1625. https://doi.org/10.1016/J.QUASCIREV.2004.02.003

Leeder, M. R., Harris, T., & Kirkby, M. J. (1998). Sediment supply and climate change: Implications for basin stratigraphy. *Basin Research*, *10*(1), 7–18. https://doi.org/10.1046/j.1365-2117.1998.00054.x

Lundberg, J., & McFarlane, D. A. (2007). Pleistocene depositional history in a periglacial terrane: A 500 k.y. record from Kents Cavern, Devon, United Kingdom. *Geosphere*, *3*(4), 199. https://doi.org/10.1130/GES00085.1

Lykousis, V., Sakellariou, D., Moretti, I., & Kaberi, H. (2007). Late Quaternary basin evolution of the Gulf of Corinth: Sequence stratigraphy, sedimentation, fault-slip and subsidence rates. *Tectonophysics*, *440*(1–4), 29–51. https://doi.org/10.1016/j.tecto.2006.11.007

Maffione, M., & Herrero-Bervera, E. (2022). A relative Paleointensity (RPI)-calibrated age model for the Corinth syn-rift sequence at IODP hole M0079A (gulf of Corinth, Greece). *Frontiers in Earth Science*, *10*, 813958. https://doi.org/10.3389/feart.2022.813958

Magny, M., Combourieu-Nebout, N., de Beaulieu, J. L., Bout-Roumazeilles, V., Colombaroli, D., Desprat, S., Francke, A., Joannin, S., Ortu, E., Peyron, O., Revel, M., Sadori, L., Siani, G., Sicre, M. A., Samartin, S., Simonneau, A., Tinner, W., Vannière, B., Wagner, B., … Wirth, S. (2013). North–south palaeohydrological contrasts in the central Mediterranean during the Holocene: Tentative synthesis and working hypotheses. *Climate of the Past*, *9*(5), 2043–2071. https://doi.org/10.5194/cp-9-2043-2013

Marini, M., Milli, S., Ravnås, R., & Moscatelli, M. (2015). A comparative study of confined vs. semi-confined turbidite lobes from the Lower Messinian Laga Basin (Central Apennines, Italy): implications for assessment of reservoir architecture. *Marine and Petroleum Geology*, *63*, 142–165. https://doi.org/10.1016/j.marpetgeo.2015.02.015

Mayall, M., & Kneller, B. (2021). Seismic interpretation workflows fordeep-water systems: A practical guide for the subsurface. *AAPG Bulletin*, *105*(11), 2127–2157. https://doi.org/10.1306/05262120094

McHargue, T. R., Hodgson, D. M., & Shelef, E. (2021). Architectural diversity of submarine lobate deposits. *Frontiers in Earth Science*, *9*, 697170. https://doi.org/10.3389/feart.2021.697170

McNeill, L. C., Shillington, D. J., Carter, G., Everest, J. D., Le Ber, E., Collier, R. E., Cvetkoska, A., De Gelder, G., Diz, P., Doan, M. L., & Ford, M. (2019a). Expedition 381 methods. https://doi.org/10.14379/iodp.proc.381.102.2019

McNeill, L. C., Shillington, D. J., Carter, G. D., Everest, J. D., Le Ber, E., Collier, R. E., Cvetkoska, A., De Gelder, G., Diz, P., Doan, M.

L., & Ford, M. (2019b). Expedition 381 summary. Proceedings of the International Ocean Discovery Program.

McNeill, L. C., Shillington, D. J., Carter, G. D. O., Everest, J. D., Gawthorpe, R. L., Miller, C., Phillips, M. P., Collier, R. E. L., Cvetkoska, A., de Gelder, G., Diz, P., Doan, M.-L., Ford, M., Geraga, M., Gillespie, J., Hemelsdaël, R., Herrero-Bervera, E., Ismaiel, M., Janikian, L., … Green, S. (2019). High-resolution record reveals climate-driven environmental and sedimentary changes in an active rift. *Scientific Reports*, *9*, 3116. https://doi.org/10.1038/s41598-019-40022-w

Milner, A. M., Müller, U. C., Roucoux, K. H., Collier, R. E. L., Pross, J., Kalaitzidis, S., Christanis, K., & Tzedakis, P. C. (2013). Environmental variability during the last interglacial: A new high-resolution pollen record from Tenaghi Philippon, Greece. *Journal of Quaternary Science*, *28*(2), 113–117. https://doi.org/10.1002/jqs.2617

Milner, A. M., Roucoux, K. H., Collier, R. E. L., Müller, U. C., Pross, J., & Tzedakis, P. C. (2016). Vegetation responses to abrupt climatic changes during the last interglacial complex (marine isotope stage 5) at Tenaghi Philippon, NE Greece. *Quaternary Science Reviews*, *154*, 169–181. https://doi.org/10.1016/j.quascirev.2016.10.016

Mitchum, R. M., Jr., Vail, P. R., & Thompson, S., III. (1977). Seismic stratigraphy and global changes of sea level: Part 2. The depositional sequence as a basic unit for stratigraphic analysis: Section 2. Application of seismic reflection configuration to stratigraphic interpretation.

Moretti, I., Sakellariou, D., Lykousis, V., & Micarelli, L. (2003). The Gulf of Corinth: An active half graben? *Journal of Geodynamics*, *36*(1–2), 323–340. https://doi.org/10.1016/S0264-3707(03)00053-X

Nixon, C. W., McNeill, L. C., Bull, J. M., Bell, R. E., Gawthorpe, R. L., Henstock, T. J., Christodoulou, D., Ford, M., Taylor, B., Sakellariou, D., & Ferentinos, G. (2016). Rapid spatiotemporal variations in rift structure during development of the Corinth rift, central Greece. *Tectonics*, *35*(5), 1225–1248. https://doi.org/10.1002/2015TC004026

Nixon, C. W., McNeill, L. C., Gawthorpe, R. L., Shillington, D. J., Michas, G., Bell, R. E., Moyle, A., Ford, M., Zakharova, N. V., Bull, J. M., & de Gelder, G. (2024). Increasing fault slip rates within the Corinth rift, Greece: A rapidly localising active rift fault network. *Earth and Planetary Science Letters*, *636*, 118716. https://doi.org/10.1016/j.epsl.2024.118716

Normandeau, A., Dietrich, P., Lajeunesse, P., St-Onge, G., Ghienne, J. F., Duchesne, M. J., & Francus, P. (2017). Timing and controls on the delivery of coarse sediment to deltas and submarine fans on a formerly glaciated coast and shelf. *Bulletin*, *129*(11-12), 1424–1441. https://doi.org/10.1130/B31678.1

Nyberg, B., Gawthorpe, R. L., & Helland-Hansen, W. (2018). The distribution of rivers to terrestrial sinks: Implications for sediment routing systems. *Geomorphology*, *316*, 1–23. https://doi.org/10.1016/j.geomorph.2018.05.007

Ott, R. F. (2020). How lithology impacts global topography, vegetation, and animal biodiversity: A global-scale analysis of mountainous regions. *Geophysical Research Letters*, *47*(20), e2020GL088649. https://doi.org/10.1029/2020GL088649

Parton, A., Clark-Balzan, L., Parker, A. G., Preston, G. W., Sung, W. W., Breeze, P. S., Leng, M. J., Groucutt, H. S., White, T. S., Alsharekh, A., & Petraglia, M. D. (2018). Middle-late quaternary palaeoclimate variability from lake and wetland deposits in the Nefud Desert, northern Arabia. *Quaternary Science Reviews*, *202*, 78–97. https://doi.org/10.1016/j.quascirev.2018.10.010

Pechlivanidou, S., Cowie, P. A., Duclaux, G., Nixon, C. W., Gawthorpe, R. L., & Salles, T. (2019). Tipping the balance: Shifts in sediment production in an active rift setting. *Geology*, *47*(3), 259–262. https://doi.org/10.1130/G45589.1

Pennos, C., Pechlivanidou, S., Modestou, S. E., Persoiu, A., Ninnemann, U. S., Gawthorpe, R. L., Maccali, J. M., Lauritzen, S. E., & Thuesen, T. (2022). Late Quaternary climatic histories from the Hermes Cave, Corinth Rift, Greece.

Pérez-Lambán, F., Peña-Monné, J. L., Badía-Villas, D., Picazo Millán, J. V., Sampietro-Vattuone, M. M., Alcolea Gracia, M., Aranbarri, J., González-Sampériz, P., & Fanlo Loras, J. (2018). Holocene environmental variability in the Central Ebro Basin (NE Spain) from geoarchaeological and pedological records. *Catena*, *163*, 147–164. https://doi.org/10.1016/j.catena.2017.12.017

Perissoratis, C., Piper, D. J. W., & Lykousis, V. (2000). Alternating marine and lacustrine sedimentation during late quaternary in the Gulf of Corinth rift basin, central Greece. *Marine Geology*, *167*(3–4), 391–411. https://doi.org/10.1016/S0025-3227(00)00038-4

Picot, M., Droz, L., Marsset, T., Dennielou, B., & Bez, M. (2016). Controls on turbidite sedimentation: Insights from a quantitative approach of submarine channel and lobe architecture (Late Quaternary Congo Fan). *Marine and Petroleum Geology*, *72*(April), 423–446. https://doi.org/10.1016/j.marpetgeo.2016.02.004

Piper, D. J. W., Hiscott, R. N., & Normark, W. R. (1999). Outcrop-scale acoustic facies analysis and latest Quaternary development of Hueneme and Dume submarine fans, offshore California. *Sedimentology*, *46*(1), 47–78. https://doi.org/10.1046/j.1365-3091.1999.00203.x

Posamentier, H. W., & Kolla, V. (2003). Seismic geomorphology and stratigraphy of depositional elements in deep-water settings. *Journal of Sedimentary Research*, *73*(3), 367–388. https://doi.org/10.1306/111302730367

Pross, J., Koutsodendris, A., Christanis, K., Fischer, T., Fletcher, W. J., Hardiman, M., Kalaitzidis, S., Knipping, M., Kotthoff, U., Milner, A. M., Müller, U. C., Schmiedl, G., Siavalas, G., Tzedakis, P. C., & Wulf, S. (2015). The 1.35-ma-long terrestrial climate archive of Tenaghi Philippon, northeastern Greece: Evolution, exploration, and perspectives for future research. *Newsletters on Stratigraphy*, *48*(3), 253–276. https://doi.org/10.1127/nos/2015/0063

Regattieri, E., Forti, L., Drysdale, R. N., Mannella, G., Hellstrom, J. C., Conati Barbaro, C., Bonacossi, D. M., & Zerboni, A. (2023). Neolithic hydroclimatic change and water resources exploitation in the Fertile Crescent. *Scientific Reports*, *13*(1), 45. https://doi.org/10.1038/s41598-022-27166-y

Roberts, N., Allcock, S. L., Barnett, H., Mather, A., Eastwood, W. J., Jones, M., Primmer, N., Yiğitbaşıoğlu, H., & Vannière, B. (2019). Cause-and-effect in Mediterranean erosion: The role of humans and climate upon Holocene sediment flux into a central Anatolian lake catchment. *Geomorphology*, *331*, 36–48. https://doi.org/10.1016/j.geomorph.2018.11.016

Roberts, N., Meadows, M. E., & Dodson, J. R. (2001). The history of mediterranean-type environments: Climate, culture and landscape. *The Holocene*, *11*(6), 631–634. https://doi.org/10.1191/09596830195663

Rohais, S., Eschard, R., Ford, M., Guillocheau, F., & Moretti, I. (2007). Stratigraphic architecture of the Plio-Pleistocene infill of the Corinth rift: Implications for its structural evolution. *Tectonophysics*, *440*(1–4), 5–28. https://doi.org/10.1016/j.tecto.2006.11.006

Rohais, S., & Moretti, I. (2017). Structural and stratigraphic architecture of the Corinth Rift (Greece): An integrated onshore to offshore basin-scale synthesis. In F. Roure, A. A. Amin, S. Khomsi, & M. A. Al Garni (Eds.), *Lithosphere dynamics and sedimentary basins of the Arabian plate and surrounding areas* (pp. 89–120). Springer International Publishing. https://doi.org/10.1007/978-3-319-44726-1

Rohling, E. J., Grant, K., Bolshaw, M., Roberts, A. P., Siddall, M., Hemleben, C., & Kucera, M. (2009). Antarctic temperature and global sea level closely coupled over the past five glacial cycles. *Nature Geoscience*, *2*(7), 500–504. https://doi.org/10.1038/ngeo557

Romans, B. W., Castelltort, S., Covault, J. A., Fildani, A., & Walsh, J. P. (2016). Environmental signal propagation in sedimentary systems across timescales. *Earth-Science Reviews*, *153*, 7–29. https://doi.org/10.1016/j.earscirev.2015.07.012

Romans, B. W., Normark, W. R., McGann, M. M., Covault, J. A., & Graham, S. A. (2009). Coarse-grained sediment delivery and distribution in the Holocene Santa Monica Basin, California: Implications for evaluating source-to-sink flux at millennial time scales. *Bulletin of the Geological Society of America*, *121*(9–10), 1394–1408. https://doi.org/10.1130/B26393.1

Roucoux, K. H., Tzedakis, P. C., Lawson, I. T., & Margari, V. (2011). Vegetation history of the penultimate glacial period (marine isotope stage 6) at Ioannina, north-west Greece. *Journal of Quaternary Science*, *26*(6), 616–626. https://doi.org/10.1002/jqs.1483

Sakellariou, D., Lykousis, V., Alexandri, S., Kaberi, H., Rousakis, G., Nomikou, P., Georgiou, P., & Ballas, D. (2007). Faulting, seismic-stratigraphic architecture and late quaternary evolution of the gulf of alkyonides basin-east gulf of Corinth, Central Greece. *Basin Research*, *19*(2), 273–295. https://doi.org/10.1111/j.1365-2117.2007.00322.x

Savoye, B., Babonneau, N., Dennielou, B., & Bez, M. (2009). Geological overview of the Angola–Congo margin, the Congo deep-sea fan and its submarine valleys. *Deep Sea Research Part II: Topical Studies in Oceanography*, *56*(23), 2169–2182. https://doi.org/10.1016/J.DSR2.2009.04.001

Schultz, P. (1998). The seismic velocity model as an interpretation asset. *Society of Exploration Geophysicists*, i–vi. https://doi.org/10.1190/1.9781560801849.fm

Sergiou, S., Geraga, M., Pechlivanidou, S., Gawthorpe, R. L., Ninnemann, U., Meckler, A. N., Modestou, S., Angelopoulou, D., Antoniou, D., Diz, P., & McNeill, L. (2024). Stratigraphic and paleoceanographic alternations within a Mediterranean semi-enclosed, syn-rift basin during marine isotope stage 5: The Gulf of Corinth, Greece. *Marine Geology*, *474*, 107340.

Shillington, D. J., McNeill, L. C., & Carter, G. D. (2018). Expedition 381 preliminary report.

Siddall, M., Rohling, E. J., Almogi-Labin, A., Hemleben, C., Meischner, D., Schmelzer, I., & Smeed, D. A. (2003). Sea-level fluctuations during the last glacial cycle. *Nature*, *423*(6942), 853–858. https://doi.org/10.1038/nature01690

Sofolabo, A. O., Dagogo, T., & Jephter, D. I. (2018). Velocity modelling using well data: Depth conversion "a case study of K-field, onshore Niger Delta area". *IOSR Journal of Applied Geology and Geophysics*, *6*(4), 18–26. https://doi.org/10.9790/0990-0604031826

Sømme, T. O., Helland-Hansen, W., Martinsen, O. J., & Thurmond, J. B. (2009). Relationships between morphological and sedimentological parameters in source-to-sink systems: A basis for predicting semi-quantitative characteristics in subsurface systems. *Basin Research*, *21*(4), 361–387. https://doi.org/10.1111/j.1365-2117.2009.00397.x

Sømme, T. O., Piper, D. J., Deptuck, M. E., & Helland-Hansen, W. (2011). Linking onshore-offshore sediment dispersal in the golo source-to-sink system (Corsica, France) during the late quaternary. *Journal of Sedimentary Research*, *81*(2), 118–137. https://doi.org/10.2110/jsr.2011.11

Spötl, C., Nicolussi, K., Patzelt, G., & Boch, R. (2010). Humid climate during deposition of sapropel 1 in the Mediterranean Sea: Assessing the influence on the Alps. *Global and Planetary Change*, *71*(3–4), 242–248. https://doi.org/10.1016/j.gloplacha.2009.10.003

Sprague, A. R., Patterson, P. E., Hill, R. E., Jones, C. R., Campion, K. M., Van Wagoner, J. C., Sullivan, M. D., Larue, D. K., Feldman, H. R., Demko, T. M., & Wellner, R. W. (2002). ABSTRACT: The physical stratigraphy of fluvial strata: A hierarchical approach to the analysis of genetically related stratigraphic elements for improved reservoir prediction. In: AAPG Annual Meeting. https://doi.org/10.1306/3fef4cc1-1741-11d7-8645000102c1865d

Spratt, R. M., & Lisiecki, L. E. (2016). A Late Pleistocene sea level stack. *Climate of the Past*, *12*(4), 1079–1092. https://doi.org/10.5194/cp-12-1079-2016

Stamatis, D., Emmanouilidis, A., Masi, A., Izdebski, A., & Avramidis, P. (2022). Holocene hydroclimatic changes in northern Peloponnese (Greece) inferred from the multiproxy record of Lake Lousoi. *Water (Switzerland)*, *14*(4), 1–12. https://doi.org/10.3390/w14040641

Stamatopoulos, L., Kamberis, E., & Alevizos, G. (2019). Detection of active fault scarps in western Peloponnese, Greece. *Quaternary International*, *508*, 88–97. https://doi.org/10.1016/J.QUAINT.2018.11.005

Stefatos, A., Papatheodorou, G., Ferentinos, G., Leeder, M., & Collier, R. (2002). Seismic reflection imaging of active offshore faults in the Gulf of Corinth: Their seismotectonic signifcance. *Basin Research*, *14*(4), 487–502. https://doi.org/10.1046/j.1365-2117.2002.00176.x

Stow, D. A. V., & Mayall, M. (2000). Deep-water sedimentary systems: New models for the 21st century. *Marine and Petroleum Geology*, *17*(2), 125–135. https://doi.org/10.1016/S0264-8172(99)00064-1

Straub, K. M., Li, Q., & Benson, W. M. (2015). Influence of sediment cohesion on deltaic shoreline dynamics and bulk sediment retention: A laboratory study. *Geophysical Research Letters*, *42*(22), 9808–9815. https://doi.org/10.1002/2015GL066131

Sweet, M. L., & Blum, M. D. (2016). Connections between fluvial to shallow marine environments and submarine canyons: Implications for sediment transfer to deep water. *Journal of Sedimentary Research*, *86*(10), 1147–1162. https://doi.org/10.2110/jsr.2016.64

Sweet, M. L., Gaillot, G. T., Jouet, G., Rittenour, T. M., Toucanne, S., Marsset, T., & Blum, M. D. (2020). Sediment routing from shelf to basin floor in the quaternary Golo system of eastern Corsica, France, western Mediterranean Sea. *GSA Bulletin*, *132*(5–6), 1217–1234. https://doi.org/10.1130/b35181.1

Sweet, M. L., Gaillot, G. T., Rittenour, T. M., Love, K., & Blum, M. D. (2021). How fast do submarine fans grow? Insights from the quaternary Golo fans, offshore Corsica. *Geology*, *49*, 1204–1208. https://doi.org/10.1130/g48911.1

Taylor, B., Weiss, J. R., Goodliffe, A. M., Sachpazi, M., Laigle, M., & Hirn, A. (2011). The structures, stratigraphy and evolution of the Gulf of Corinth rift, Greece. *Geophysical Journal International*, *185*(3), 1189–1219. https://doi.org/10.1111/j.1365-246X.2011.05014.x

Tofelde, S., Bernhardt, A., Guerit, L., & Romans, B. W. (2021). Times associated with source-to-sink propagation of environmental signals during landscape transience. *Frontiers in Earth Science*, *9*, 1–51. https://doi.org/10.3389/feart.2021.628315

Tucker, G. E., McCoy, S. W., Whittaker, A. C., Roberts, G. P., Lancaster, S. T., & Phillips, R. (2011). Geomorphic significance of postglacial bedrock scarps on normal-fault footwalls. *Journal of Geophysical Research: Earth Surface*, *116*(1), 1–14. https://doi.org/10.1029/2010JF001861

Turnbull, L., Wainwright, J., & Brazier, R. E. (2009). Changes in hydrology and erosion over a transition from grassland to shrubland. *Hydrological Processes*, *24*, 414. https://doi.org/10.1002/hyp.7491

Tzedakis, P. C. (1994). Vegetation change through glacial-interglacial cycles: A long pollen sequence perspective. *Philosophical Transactions of the Royal Society, B: Biological Sciences*, *345*(1314), 403–432. https://doi.org/10.1098/rstb.1994.0118

Tzedakis, P. C., Hooghiemstra, H., & Pälike, H. (2006). The last 1.35 million years at Tenaghi Philippon: Revised chronostratigraphy and long-term vegetation trends. *Quaternary Science Reviews*, *25*(23–24), 3416–3430. https://doi.org/10.1016/j.quascirev.2006.09.002

Wang, Y., Straub, K. M., & Hajek, E. A. (2011). Scale-dependent compensational stacking: An estimate of autogenic time scales in channelized sedimentary deposits. *Geology*, *39*(9), 811–814. https://doi.org/10.1130/G32068.1

Watkins, S. E., Whittaker, A. C., Bell, R. E., McNeill, L. C., Gawthorpe, R. L., Brooke, S. A. S., & Nixon, C. W. (2018). Are landscapes buffered to high-frequency climate change? A comparison of sediment fluxes and depositional volumes in the Corinth rift, central Greece, over the past 130 k.y. *Bulletin Geological Society of America*, *131*, 372–388. https://doi.org/10.1130/B31953.1

Wei, D., González-Sampériz, P., Gil-Romera, G., Harrison, S. P., & Prentice, I. C. (2021). Seasonal temperature and moisture changes in interior semi-arid Spain from the last interglacial to the Late Holocene. *Quaternary Research*, *101*, 143–155. https://doi.org/10.1017/qua.2020.108

Wynn, R. B., Kenyon, N. H., Masson, D. G., Stow, D. A., & Weaver, P. P. (2002). Characterization and recognition of deep-water channel-lobe transition zones. *AAPG Bulletin*, *86*(8), 1441–1462. https://doi.org/10.1306/61eedcc4-173e-11d7-8645000102c1865d

Xoplaki, E., González-Rouco, J. F., Luterbacher, J., & Wanner, H. (2004). Wet season Mediterranean precipitation variability: Influence of large-scale dynamics and trends. *Climate Dynamics*, *23*(1), 63–78. https://doi.org/10.1007/s00382-004-0422-0

Zhou, W., Chiarella, D., Zhuo, H., Wang, Y., Tang, W., Zou, M., & Xu, Q. (2021). Genesis and evolution of large-scale sediment waves in submarine canyons since the Penultimate Glacial Maximum (ca. 140 ka), northern South China Sea margin. *Marine and Petroleum Geology*, *134*, 105381. https://doi.org/10.1016/j.marpetgeo.2021.105381

SUPPORTING INFORMATION

Additional supporting information can be found online in the Supporting Information section at the end of this article.

How to cite this article: Mohamed, M. A., Collier, R. E. L., Hodgson, D. M., Gawthorpe, R. L., Shillington, D. J., Muravchik, M., & Sakellariou, D. (2024). Sediment flux variation as a record of climate change in the Late Quaternary deep-water active Corinth Rift, Greece. *Basin Research*, *36*, e12896. https://doi.org/10.1111/bre.12896